UCLouvain

École polytechnique de Louvain

Investigation and mitigation of dispersion errors in a Navier-Stokes solver with variable resolution

Author: **Florian De Bel**
Supervisor: **Grégoire Winckelmans**
Readers: **Yann Bartosiewicz, Jean-François Remacle**
Academic year 2023–2024
Master [120] in Mathematical Engineering

To whom it may concern,

Thanks to my supervisor Prof. Grégoire Winckelmans, who taught me most of my knowledge in fluid mechanics and who guided me throughout this master's thesis. Thanks to the readers Prof. Yann Bartosiewicz and Prof. Jean-François Remacle for their time spent reading.

This master's thesis is a page that turns in my life. A page, or rather sixty pages, that conclude my civil engineering studies in applied mathematics. But also all those good years in which I met wonderful people, whether through personal projects or through my studies.

I would like to thank all the people who helped me to get to where I am today and to achieve this master's thesis.

Florian

Contents

1 Introduction **1**

2 Navier-Stokes solver **3**

2.1 Mathematical formulation 3

2.2 Spatial discretization 5

2.3 Case study : Flow past a cylinder 9

2.4 Case study : Poiseuille flow 13

3 Two Gaussian vortices in a periodic box **15**

3.1 Case presentation 15

3.2 Analysis of the uniform results 19

3.3 Verification of the diffusion term 23

3.4 Analysis of the non-uniform results 25

3.5 Case variation : Angle of incidence with the mesh 30

4 Mitigation of the error due to non-uniform mesh resolution **32**

4.1 Introduction to the mitigation model 32

4.2 Further analysis of hyperdiffusion 34

4.3 Application of the model to our DNS solver 37

4.4 Analysis of the mitigation model results 38

4.5 Analysis when increasing the order of the mitigation model 43

5 Four Gaussian vortices in a periodic box **46**

5.1 Case presentation 46

5.2 Analysis of the uniform results 49

5.3 Analysis of the non-uniform results with mitigation model 51

6 Conclusion and perspectives **56**

A Complete non-uniform discretization of the convection and diffusion terms 58

B Modal analysis of the second order finite difference schemes for first and second order derivatives 60

C Complete discretization of the mitigation model for $N = 4$ and $N = 6$ for a finite difference solver with a non-uniform grid 64

Bibliography 66

Abbreviations and Symbols

Abbreviation	**Meaning**
DNS	Direct Numerical Simulation
LES	Large Eddy Simulation
NS	Navier-Stokes equations
CD_x	Second order central finite difference of the x derivative

Symbol	**Units**	**Meaning**
$\hat{\cdot}$	[−]	Frequency domain quantity
$\tilde{\cdot}$	[−]	Dimensionless quantity
$\bar{\cdot}$	[−]	Filtered quantity
∂	[−]	Partial derivative
δ	[−]	Discrete derivative
x, y	[m]	Horizontal and vertical position in the "physical space"
u, v	[m/s]	Velocity in the x and y direction
ω	[rad/s]	Vorticity in the z direction
Re	[−]	Reynolds number
CFL	[−]	Courant-Friedrichs–Lewy condition
ν	[m^2/s]	Kinematic viscosity
P	[m^2/s^2]	Kinematic pressure
Φ	[m^2/s^2]	Modified pressure
ψ	[m^2/s]	Streamfunction
$\mathbf{H}_h$	[m/s^2]	Space discretization of the convective term
Γ_0	[m^2/s]	Initial circulation of the Gaussian vortex
σ_0	[m]	Parameter controlling the radius of the Gaussian vortex
r_c	[m]	Distance at which the Gaussian vortex has maximum velocity
b_0	[m]	Spacing between the two primary vortices
ξ, η	[m]	Horizontal and vertical position in the "numerical space"
Δ	[m]	Variable space step size depending on the position
Δ_c, Δ_f	[m]	Coarsest and finest space step size
Δ_ξ, Δ_η	[m]	Horizontal and vertical space step size in the "numerical space"
h	[m]	Space step size for uniform zone or uniform simulation
Δt	[s]	Integration timestep
α	[deg]/[m^4/s]	Angle of incidence with mesh/Hyperdiffusion of order 4 coefficient
E_2, E_∞	[−]	2- and ∞-norm error
C	[−]	Coefficient of the mitigation model

Chapter 1

Introduction

We live in a world where interactions with fluids are everywhere. The recent studies on fluid mechanics involve a lot of different subjects: ocean currents [1], wakes of an airplane [2], blood flow in the cardiovascular system [3], wind blowing between buildings [4], vortex interaction with the ground [5] and many others. If we want to understand the movement and the evolution of all these fluids, we need to study them. However, full-scale experiments are not always possible. We must therefore analyze the equations that represent these fluids. We will focus here on the Navier-Stokes equations, one of the famous Millennium Prize problems introduced by the Clay Foundation [6]. As there is no known analytical solution, numerical methods are the only remaining solution. Several methods exist to discretize the problem such as finite differences, finite elements, finite volumes, spectral methods, particle methods or meshless methods [7]. Here we will concentrate on the finite difference method, which is perhaps the simplest to understand and to analyze. To correctly simulate the fluid around aerodynamic profiles such as airplanes, you need to discretize with a lot of points. Calculations quickly become impossible to capture the smaller scales at which dissipation occurs, the Kolmogorov scales [8]. We can therefore use non-uniform resolutions that will allow us to place more points in the boundary layer, where the variations are the greatest, and fewer points far from the profiles, where the flow undergoes smaller variation. These types of grids will generate additional errors due to the non-uniformity of the discretization. In particular, when information passes from a well resolved zone to a less well resolved zone, there is a net loss of information and an associated error.

In general, the errors generated by the non-uniformity of the mesh are ignored. However, it's easy to understand that when the solution goes from a fine mesh to a coarse mesh, or from a coarse mesh to a fine mesh, information is lost or created, but we know that the information transmitted may be incorrect. Here, we will be concentrating on mesh coarsening, since it is the one that generates the most errors. In this case, information is lost, the solver manifests these errors with a wrong diffusion or a wrong convection of the frequency modes. In most cases, these errors are observed in the form of oscillations. Most of the time we just increase the resolution or the order of the solver. However, sometimes this is impossible due to limited computing resources. In this master's thesis, we will focus on these often overlooked dispersion errors, analyze them and try to correct them with an mitigation term. We will assess the effectiveness

of attenuation to determine if it warrants further investigation and if it might be beneficial to include the mitigation term in the professional solver.

Our analysis will be based on a 2D direct numerical simulation (DNS) solver of the Navier-Stokes equations using finite difference methods, which allows the use of variable resolution. This solver will be developed entirely from scratch for this master's thesis. The complete formulation and the discretization will be explained in the next chapter. Next, we will apply this solver to a textbook case, the convection of a Gaussian vortex, where variable resolution produces a quantifiable error. We will analyze the results and observe the dispersion errors. This case will be developed in detail in the chapter "Two vortices in a periodic box". Next, we will try to mitigate the dispersion errors. We will use a model presented in the paper [9] which is used for commutation errors generated in a variable resolution LES solver. The aim is to see whether this model, based on a hyperdiffusion term, is applicable to our the DNS case. Detailed analysis of this model and its application to the vortex dipole case will be presented in the chapter entitled "Mitigate of the error due to non-uniform mesh resolution". Finally, in the last chapter, we will apply the mitigation model to a more complex case with a wider range of scales to see if it still behaves correctly. In this case, two secondary vortices will be added to generate interaction with the primary vortices. Two cases will be studied, one for each possible direction of rotation of the secondary vortices.

To summarize the four main objectives of this master's thesis are:

- Building a 2D finite difference Navier-Stokes solver with variable resolution that will enable us to analyze and observe dispersion errors.
- Investigating the dispersion errors generated by the non-uniform resolution in a well-chosen test case.
- Redeveloping the model proposed for LES commutation error in the paper [9] to apply it to our DNS solver and try to attenuate the dispersion errors initially observed.
- Finding a new case to validate the mitigation model on cases with a wider range of scales.

Chapter 2

Navier-Stokes solver

This chapter introduces the 2D Navier-Stokes solver developed in this master's thesis. The developed finite differences solver can use a non-uniform discretization in both directions. This will allows us to observe the dispersion error that we will later try to mitigate. The method used, the temporal scheme and the spatial discretization are presented here. The chapter also contains two cases that have been tested to show the good performance of the solver.

2.1 Mathematical formulation

First, let's introduce the system on which we will work. This is the incompressible Navier-Stokes equations given by

$$\nabla \cdot \mathbf{v} = 0 \tag{2.1}$$

$$\frac{\partial \mathbf{v}}{\partial t} + (\mathbf{v} \cdot \nabla)\mathbf{v} = -\nabla P + \nu \Delta \mathbf{v} \tag{2.2}$$

where $\mathbf{v}$ is the velocity vector, $\nu = \frac{\mu}{\rho}$ the kinematic viscosity and $P = \frac{p - p_{ref}}{\rho}$ the kinematic pressure.

Recall that the conservation of mass, Equation 2.1, is not an evolutionary equation because it does not involve time. This equation should hold in all places and at all times. Pressure will ensure this condition. To integrate in time the momentum equation, Equation 2.2, and guarantee the conservation of mass at each timestep, a two step projection is used [10]. The time integration is done with the classical Explicit Euler scheme (EE) for all terms except the convective term. The latter is generally the more unstable, since the convection modes on to the imaginary axis where explicit integration methods are less stable. We use a second order Adams-Bashforth scheme (AB2) because its stability region is tangent to the imaginary axis. Note that we will still use the Explicit Euler scheme for the first timestep. The stability region of both schemes is shown in the Figure 2.1. The Euler Explicit scheme is of order $\mathcal{O}(\Delta t)$ and the Adams-Bashford scheme is of order $\mathcal{O}(\Delta t^2)$.

$$(EE) => u_i^{n+1} = u_i^n + f(x_i, t^n)\Delta t$$

$$(AB2) => u_i^{n+1} = u_i^n + \left(\frac{3}{2}f(x_i, t^n) - \frac{1}{2}f(x_i, t^{n-1})\right)\Delta t$$

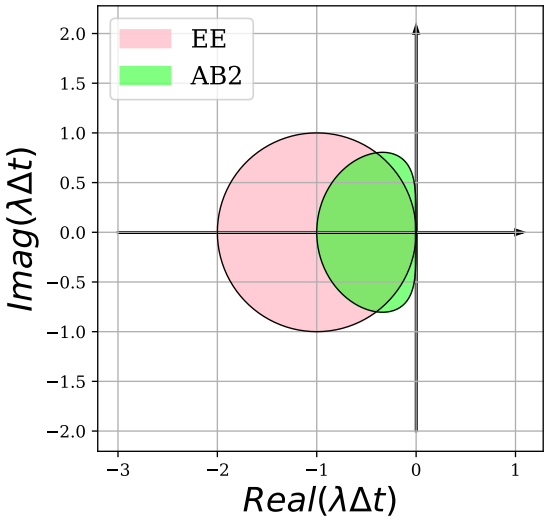

Figure 2.1: *Stability region of Explicit Euler (EE) and Adams-Bashforth 2 (AB2) temporal scheme.*

The simulation is done in four steps, first we integrated the momentum equation in time, the convective term is denoted by the symbol $\mathbf{H}_h$. Then we solve a Poisson equation to find the modification of the pressure we need to apply to ensure mass continuity. This modification is called the modified pressure and is denoted by the letter Φ. We then correct the velocity and pressure such that mass continuity is ensured at the end of each timestep. The formulation of the four substeps of a timestep is presented below, in Equations 2.3 to 2.6.

$$\frac{\mathbf{v}^* - \mathbf{v}^n}{\Delta t} = -\frac{1}{2}(3\mathbf{H}_h^n - \mathbf{H}_h^{n-1}) - \nabla_h P^n + \nu\nabla_h^2\mathbf{v}^n \tag{2.3}$$

$$\nabla_h^2\Phi = \frac{1}{\Delta t}\nabla_h \cdot \mathbf{v}^* \tag{2.4}$$

$$\frac{\mathbf{v}^{n+1} - \mathbf{v}^*}{\Delta t} = -\nabla_h\Phi \tag{2.5}$$

$$P^{n+1} = P^n + \Phi \tag{2.6}$$

The Poisson equation, Equation 2.4, which appears to compute the modified pressure, is solved using the PETSc library [11]. The solver used is an LU direct solver, which allows parallelization on multiple CPUs. Note that the matrix is quite sparse, matrix density $<<$ 1%. Therefore,

it is important to deal with the sparsity of the matrix to save time and memory. A sparse memory containing only non-zero values allows us to save a lot of memory and a solver that takes sparsity into account is also important to save execution time. This is already implemented and well-treated in the PETSc library.

2.2 Spatial discretization

In this section, we will explain the grid used and the non-uniform discretization of the solver. The spatial discretization is done using a staggered MAC (Marker-And-Cell) mesh [12, 13]. As shown in Figure 2.2a, this means that pressure points and velocity points are not collocated. The advantages of the MAC mesh are :

- Pressure and velocity points are decoupled by construction
- Conservation of mass within a cell is easy to check at any time.
- Boundary can be easily represented with ghost point, Figure 2.2b
- Oscillations in the solution are reduced as variations are not considered at the same point.
- Pressure and vorticity are easier to compute

The major drawback is that it can be tricky to handle quantities that are not in the same location. Managing those at half indices, such as $i + 1/2$, can be particularly challenging, especially for the nonlinear convective term. If readers are interested by trying a similar code, indices will be one of the main challenges.

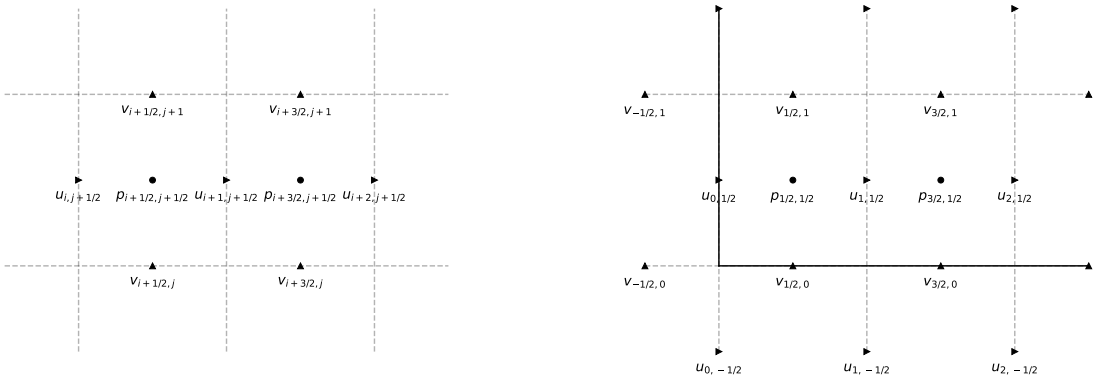

(a) *General case* ***(b)*** *Boundary region*

Figure 2.2: *Marker-And-Cell (MAC) mesh.*

Second order spatial finite difference schemes are used throughout the solver. The order of the solver is verified in the next chapter for the uniform case. The scheme is given here for the first and second order derivatives. Note that the notation ∂ is used when we are dealing with the actual quantity required, we will use δ for the discretized quantity. The notation h is used for the distance between two points when the resolution is uniform.

$$\left.\frac{\delta u}{\delta x}\right|_i = \frac{u_{i+1} - u_{i-1}}{2h} + \mathcal{O}(h^2)$$

$$\left.\frac{\delta^2 u}{\delta x^2}\right|_i = \frac{u_{i+1} - 2u_i + u_{i-1}}{h^2} + \mathcal{O}(h^2)$$

The discretization of the Navier-Stokes equations is conservative because the mass, pressure, and viscous terms are conserved a priori since these terms appear in the divergence form, [14]. The convective term is also conserved when written in divergence form. This term can be written in three forms: divergence, advective, and skew-symmetric.

$$(Div)_i = \frac{\partial(u_j u_i)}{\partial x_j}$$

$$(Adv)_i = u_j \frac{\partial u_i}{\partial x_j}$$

$$(Skew)_i = \frac{1}{2}(Div)_i + \frac{1}{2}(Adv)_i$$

Divergence and advective forms are connected with each other through

$$(Adv)_i = (Div)_i - u_i(Cont)$$

where $(Cont) = \frac{\partial u_i}{\partial x_i}$, is the mass continuity term. All forms are conservative if the continuity equation is satisfied. A first paper [14], presents high order schemes with conservation properties in discrete sense. The later paper, [15] generalized this to non-uniform meshes while preserving discrete conservation. The latter is what we focus on in this master's thesis.

Our code will allow non-uniform grid spacing in both directions. A mapping is needed from the "numerical space" in (ξ,η) where the resolution is uniform to the "physical space" in (x,y) where the resolution is non-uniform, see Figure 2.3. The grid and the cells will still have a rectangular shape because we will decouple the mapping in x and in y. We will have two mapping functions, one from ξ to x defined by the function $x = f(\xi)$ and the other from η to y defined by the function $y = g(\eta)$. We can define Δ_ξ and Δ_η as the uniform grid space in the "numerical space". We will only consider mapping functions that have a domain from $[0, L]$ to $[0, L]$, for the simplicity of the mapping function. As explained we will treat x and y separately, so the derivative of the mappings will be also decoupled.

$$\frac{dx}{d\xi} = f'(\xi) \qquad\qquad \frac{dy}{d\eta} = g'(\eta)$$

In the "physical space" derivatives of a quantity will become

$$\frac{\partial \phi}{\partial x} = \frac{\partial \xi}{\partial x}\frac{d\phi}{d\xi} = \frac{1}{Jx}\frac{\partial \phi}{\partial \xi}$$

$$\frac{\partial \phi}{\partial x} = \frac{\partial \eta}{\partial y}\frac{d\phi}{d\eta} = \frac{1}{Jy}\frac{\partial \phi}{\partial \eta}$$

where Jx and Jy are Jacobians of the transformation and there numerical discretization follow

$$Jx(\xi_i) \approx \left.\frac{\delta x}{\delta \xi}\right|_i = \frac{x_{i+1/2} - x_{i-1/2}}{\Delta_\xi}$$

$$Jy(\eta_j) \approx \left.\frac{\delta y}{\delta \eta}\right|_j = \frac{y_{j+1/2} - y_{j-1/2}}{\Delta_\eta}$$

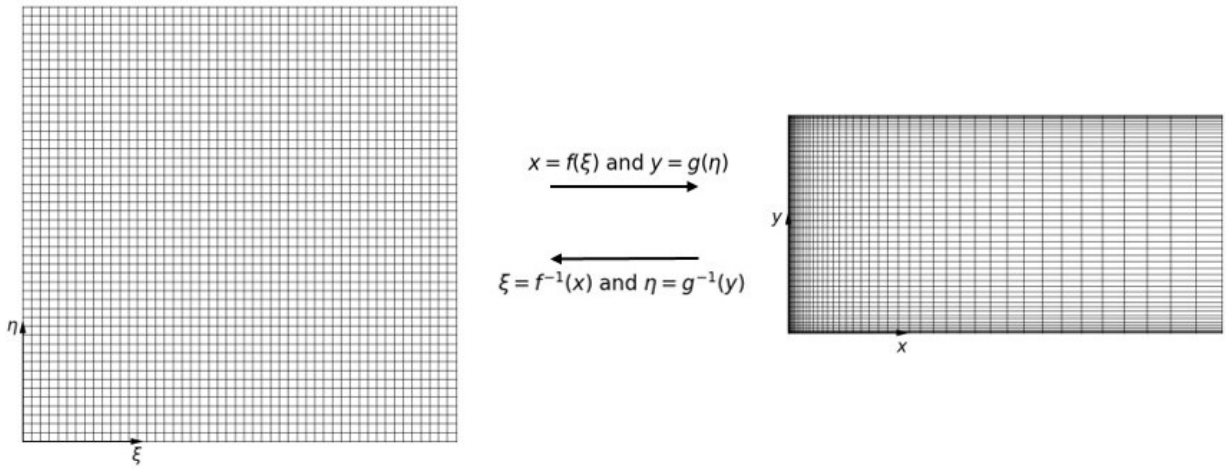

Figure 2.3: *Mapping between the numerical (left) and physical (right) domains.*

Now, we are going to develop the convection and diffusion terms for a non-uniform discretization. First we will introduce some notations that will be used throughout this section the shorter the notation. We will write x, y, ξ, η respectively as x_1, x_2, ξ_1, ξ_2. The finite difference operator of stencil n and the interpolation operator can be developed as

$$\frac{\delta_n \phi}{\delta_n \xi_1} = \frac{\phi(\xi_1 + n\Delta_{\xi_1}/2, \xi_2) - \phi(\xi_1 - n\Delta_{\xi_1}/2, \xi_2)}{n\Delta_{\xi_1}} \tag{2.7}$$

$$\overline{\phi}^{n\xi_1} = \frac{\phi(\xi_1 + n\Delta_{\xi_1}/2, \xi_2) + \phi(\xi_1 - n\Delta_{\xi_1}/2, \xi_2)}{2} \tag{2.8}$$

The dicretization presented by the paper [15] for the second order scheme of the convective term follow

$$(Div)_i = \frac{1}{Jx_j(\xi_j)} \frac{\delta_1 \overline{u_j}^{1x_i} \overline{u_i}^{1x_j}}{\delta_1 \xi_j}$$

$$(Adv)_i = \overline{\overline{u_j}^{1\xi_i} \frac{1}{Jx_j(\xi_j)} \frac{\delta_1 u_i}{\delta_1 \xi_j}}^{1\xi_j}$$

$$(Skew)_i = \frac{1}{2}(Div)_i + \frac{1}{2}(Adv)_i$$

Note that in the non-uniform case there is a commutation term between the advective and the divergence form, Equation 2.9. Thus, the divergence form is the only one that preserves momentum even when continuity is enforced. We will choose the skew-symmetric form as a further analysis which was done in the source paper [15], found that it was the only form that conserved the kinematic energy.

$$(Adv)_i = (Div)_i - u_i \overline{(Cont)}^{1x_i} + u_i \left[\overline{\frac{\delta_1 u_i}{\delta_1 x_i}}^{1x_i} - \frac{\delta_1 \overline{u_i}^{1x_i}}{\delta_1 x_i} \right] \tag{2.9}$$

For the diffusive term we will use the discretization presented in the paper [16]

$$(Diff)_i = \frac{2}{(Jx_j(\xi_{j+1/2}) + Jx_j(\xi_{j-1/2}))} \frac{\delta_1}{\delta_1 \xi_j} \left(\frac{1}{Jx_j(\xi_j)} \frac{\delta_1 u_i}{\delta_1 \xi_j} \right)$$

All developed discretizations of the convective and diffusive terms are provided in Appendix A.

2.3 Case study : Flow past a cylinder

First, an assessment of the solver was conducted in a uniform case, focusing on the classical case of flow past a cylinder. To take in account the geometry of the cylinder, a penalization method was used [17]. This involved modifying Equation 2.3 by introducing a new term resulting in Equation 2.10. The new variable χ is binary, taking a value 1 within the solid region and 0 within the flow. $\Delta\tau$ is a time parameter for the penalization, one can take $\frac{\Delta t}{\Delta\tau} = 10^3$ to have a good representation of the body, without requiring to reduce the timestep of the simulation to be stable. The larger the ratio is the better the presence of the body is taken into account but also the more you pay on your timestep. Note that the velocity $\mathbf{v}_s^{n+1}$ corresponds to the velocity of the solid body, this formulation allows us to generate a rotation of the body.

$$\frac{\mathbf{v}^* - \mathbf{v}^n}{\Delta t} = -\frac{1}{2}(3\mathbf{H}_h^n - \mathbf{H}_h^{n-1}) - \nabla_h P^n + \nu\nabla_h^2\mathbf{v}^n - \chi\frac{\mathbf{v}^* - \mathbf{v}_s^{n+1}}{\Delta\tau} \tag{2.10}$$

The boundary conditions are set such that at the inflow, $u = U_\infty$ and $v = 0$. Due to the staggered mesh, Figure 2.2b, a ghost point is used with Equation 2.11 to impose the real value on the boundary ($v_\Gamma = 0$) while the preserving second order in space. At the outflow, linear transport equations are solved for u and ω to impose the velocity values at the boundary, according to Equation 2.12. This ensures that mass conservation is maintained and that the inflow and outflow contributions are equal. The top and bottom boundaries are assumed to be inviscid, i.e., with no-through flow ($v = 0$) and zero vorticity ($\omega = 0$).

$$v_0 = -\frac{1}{5}(v_3 - 5v_2 + 15v_1 - 16v_\Gamma) \tag{2.11}$$

$$\begin{cases} \frac{\partial u}{\partial t} + U_\infty\frac{\partial u}{\partial x} = 0 \\ \frac{\partial \omega}{\partial t} + U_\infty\frac{\partial \omega}{\partial x} = 0 \end{cases} \tag{2.12}$$

The case is characterized by a dimensionless number called the Reynolds number, which is given by relation $Re = \frac{U_\infty D}{\nu}$. Two cases are tested here $Re = 100$ and $Re = 10000$.

In the first case, $Re = 100$, the cylinder rotates slowly at the beginning to break the symmetry (a dimensionless angular velocity of $\frac{\omega_s D}{U_\infty} = 10^{-2}$ up to a dimensionless time of $\tilde{t} = \frac{tU_\infty}{D} = 10$) and to induce shedding in a shorter period of time. The results are shown in Figure 2.4, we see that two recirculation zones are created behind the cylinder. Then, around $\tilde{t} = \frac{tU_\infty}{D} = 25$, the artificial asymmetry created by the rotation of the cylinder starts its work and some oscillations start to appear. Finally, a first vortex is shed and we then observe the classical Von Karman vortices in the shedding [18].

In the case at $Re = 10000$, the computational cost is more important because we have more small structures to capture, in other words, more scale to resolve. The computational domain is reduced because the timestep and the space discretization needed are quite low. Even with these changes, the simulation takes almost a day on an 8CPU laptop. Dimensionless numbers used to control the resolution of the simulation follow a mesh Reynolds number of $Re_h = \frac{(|u|+|v|)h}{\nu} < 80$,

a mesh Reynolds based on the vorticity of $Re_{h,\omega} = \frac{|\omega|h^2}{\nu} < 60$ and a Courant–Friedrichs–Lewy condition of $CFL = 0.15$. These values are still quite large. As a result, we see that there are instabilities at the beginning of the boundary layer. This tells us that the flow is coarsely resolved. In the shedding, we can observe more complex behavior than in the lower Re case. The recirculation zone has eddies of smaller size. Similar results were found in papers [19, 20] where $Re = 9500$ was investigated.

The goal of this simulation was to demonstrate the validity of the uniform code and to show that with a relatively straightforward code developed from scratch we can produce some interesting 2D fluid simulations.

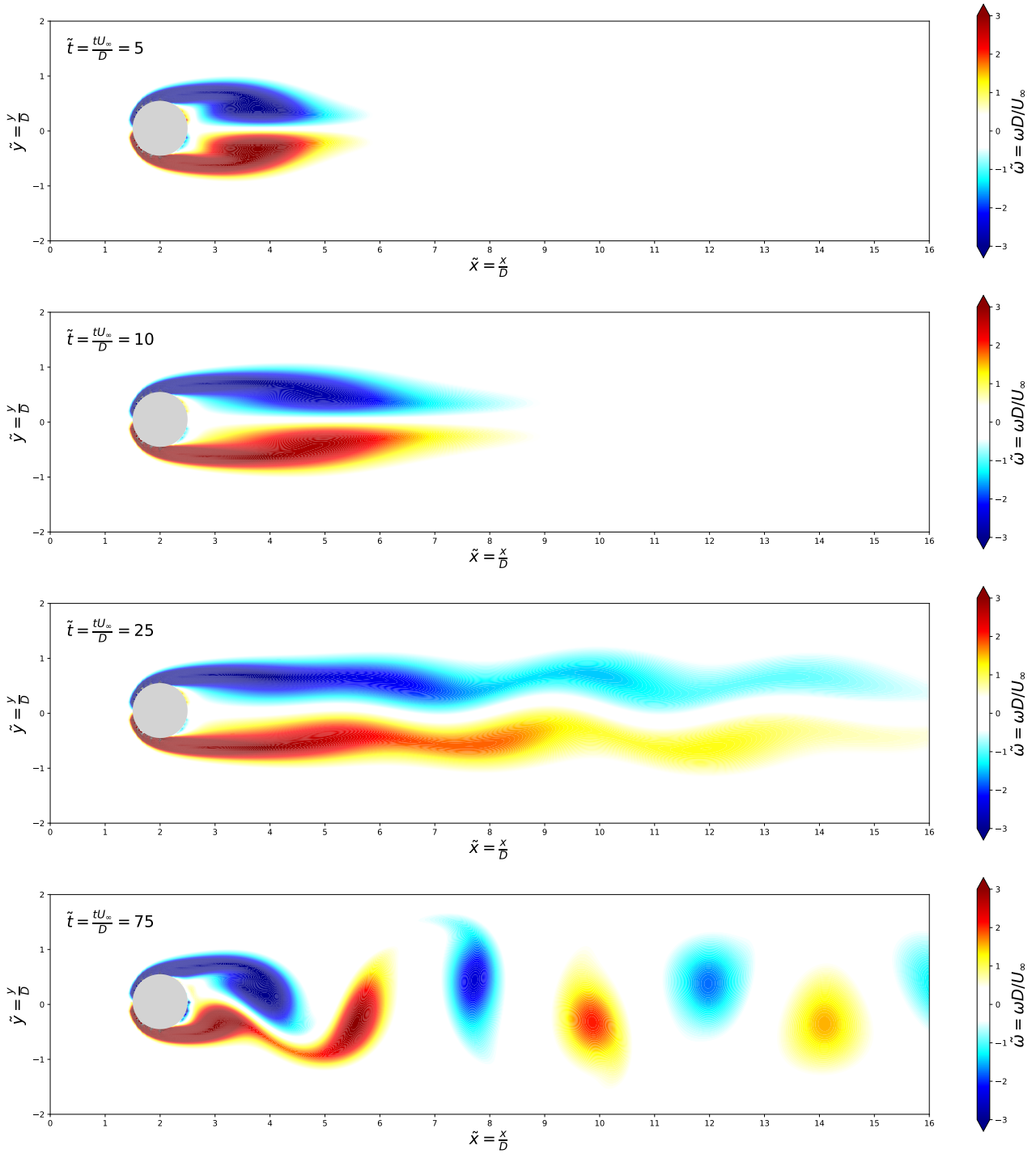

Figure 2.4: *The dimensionless vorticity of shedding past a cylinder at* $Re = 100$*. The color plot is saturated at* $|\tilde{\omega}| > 3$*.*

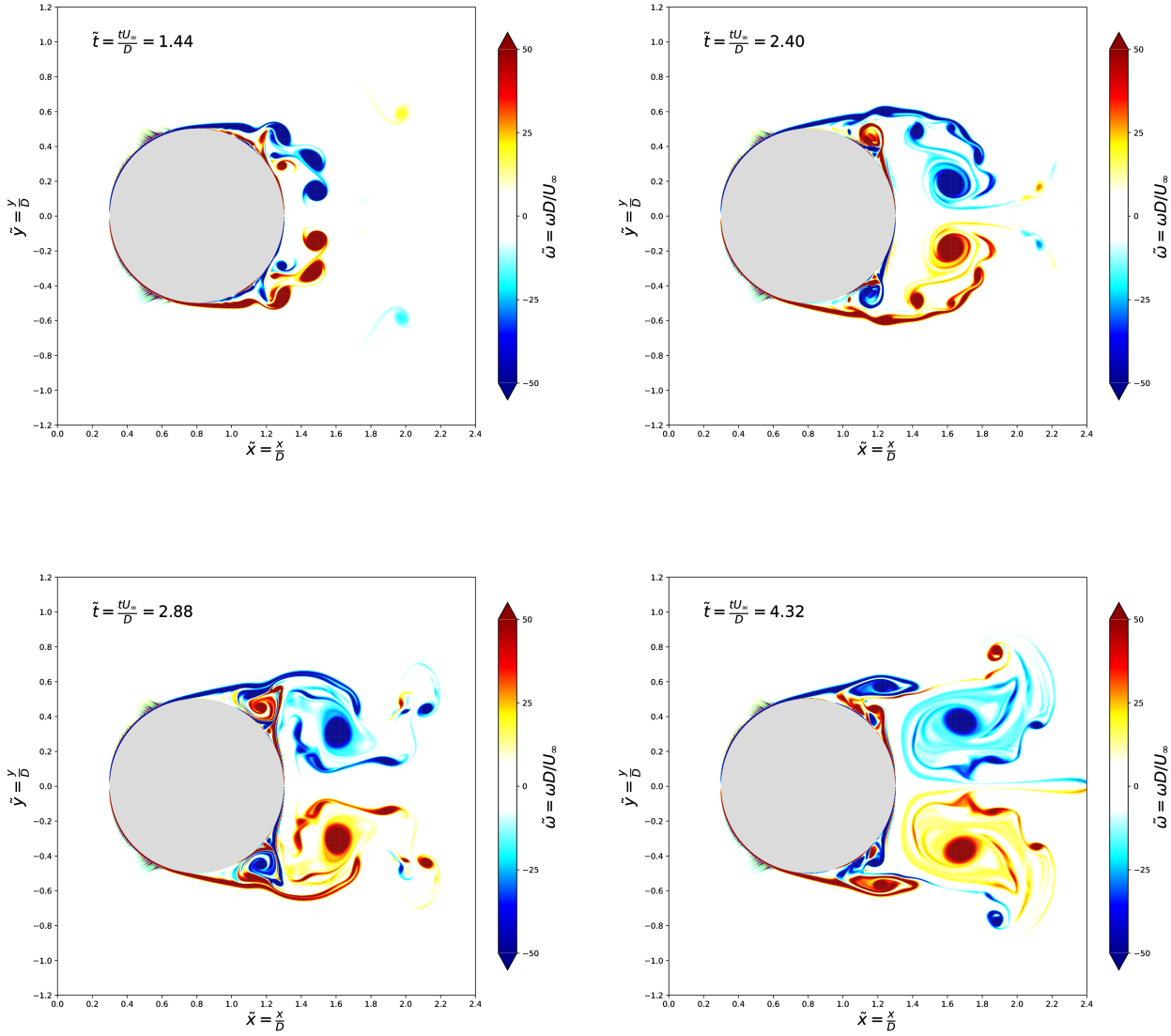

Figure 2.5: *The dimensionless vorticity of a flow past a cylinder at* $Re = 10000$*. The color plot is saturated at* $|\tilde{\omega}| > 50$*.*

2.4 Case study : Poiseuille flow

To validate the code and in particular the implementation of the non-uniform discretization, we can simulate the well-known case, Poiseuille flow between two infinite plates [21]. The case should have a periodic condition in x and no-slip boundary condition in $y = H$ and $y = -H$ that representing the plates. We then start with $u_0 = U_\infty$ in the whole domain. By doing this, no matter what the initial condition, the velocity will fall to 0. To obtain the Poiseuille flow, we need to have a pressure gradient in the streamwise direction x. We will then recreate this pressure gradient by applying a forcing term as follow

$$\frac{dP_f}{dx} = -3Re\frac{\nu^2}{H^3}$$

where $Re = \frac{U_m H}{\nu}$ is the Reynolds number based on U_m the center velocity. Now, we have everything we need to run the uniform case. For the mapping between the "numerical" and "physical domains", we will use the hyperbolic tangent mapping function. This function is written in Equation 2.13 where β is a parameter that we can tune to choose the profile of the mapping function and and shown in Figure 2.7. This is typically used to solve turbulent boundary layers in 3D, as it puts more points close to the wall and allows us to get a better resolution of the quantity variation.

$$y = g(\eta) = 0.5\Big(1 - \frac{\tanh(\beta(1-2\eta))}{\tanh(\beta)}\Big) \tag{2.13}$$

The analytical profile of a Poiseuille flow is

$$\frac{u(y)}{U_m} = \frac{3}{2}\Big(1 - \Big(\frac{y}{H}\Big)^2\Big)$$

where U_m is the flow velocity defined by $U_m = \frac{Q}{2H} = \frac{H^2}{3\nu}(-\frac{dP}{dx})$. Note that the dimensionless profile is independent of the Reynolds number.

Both the uniform and the non-uniform (using $\beta = 1$ here) cases converge to the analytical solution, as shown in Figure 2.6. This has been demonstrated by calculating the maximum errors compared to the analytical solution calculated with Equation 2.14. Note also that the solution is symmetric so this is a good case to check the implementation of the solver. The simulation was also run in y to check the indices in both directions.

$$E_{max} = \frac{||u_{compute} - u_{analytic}||_\infty}{U_m} \tag{2.14}$$

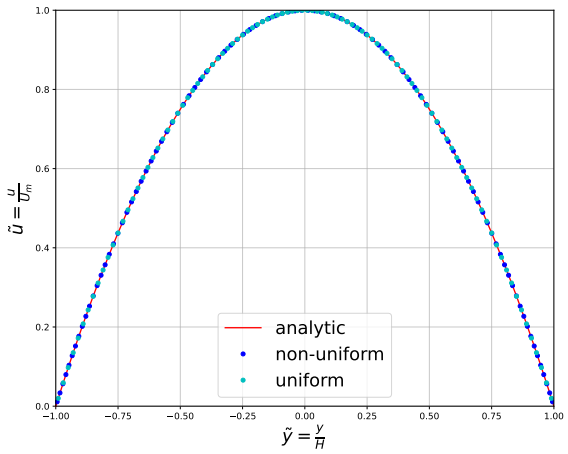

Figure 2.6: *Poisseuille flow velocity profile as a function of the dimensionless length.*

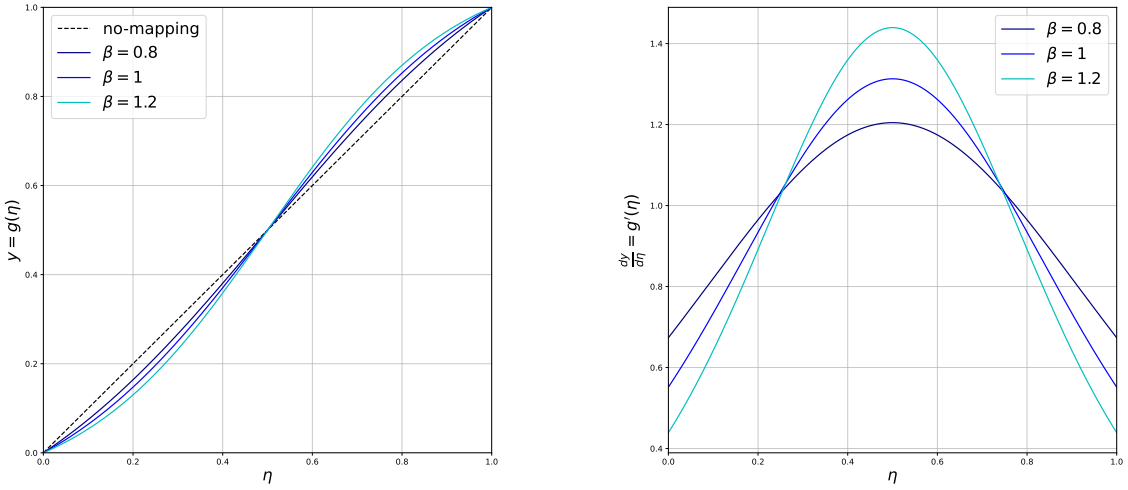

(a) *Mapping function* ***(b)*** *Derivative of the mapping function*

Figure 2.7: *Hyperbolic tangent mapping function and derivative of the mapping function.*

Chapter 3

Two Gaussian vortices in a periodic box

For the deep analysis of this master's thesis, we wanted a case where we can check the good working of the non-uniform solver and where we can find a dispersion error pattern while coarsening the resolution. We chose to analyze a Gaussian vortex convection so that some analytical results exist to support the analysis.

Remembering that we are working within a finite domain and that a vortex holds infinite support for the velocity field, as shown Figure 3.2. One cannot physically simulate a vortex inside a box using a velocity-pressure code with realistic boundary conditions. This is where the idea of periodic boundary conditions has emerged, as they make the domain infinite. However, to achieve a periodic domain, we need zero circulation within our initial box. One way to impose this condition is to consider two vortices of opposite circulation within this periodic box. Another advantage of this case is that the pair of vortices will induce a velocity field that will cause them to move. This eliminates the need to impose a convection velocity, U_∞. Furthermore, a pair of Gaussian vortices is essentially analogous to the structure of the two vortices system that is shed by lifting surfaces such as wings and rotors when fully rolled up, a phenomenon studied at the Thermodynamics and FLuid divison (TFL) of UCLouvain, [22–24].

3.1 Case presentation

In this first section, we will introduce the case. Since the analytical results are well known, we choose to work with Gaussian vortices instead of other vortex shapes, this shape of vortex is sometimes called the Lamb-Oseen vortex [25, 26]. The initial condition imposed at time 0 takes the form of the Equation 3.1. This means two Gaussian vortices of opposite circulations, one with circulation $-\Gamma_0$ in $(-0.5b_0, 0)$ and the other with circulation Γ_0 in $(0.5b_0, 0)$. The periodic box thus has a circulation of 0, as desired. The case is shown in Figure 3.1. The two vortices are thus separated by a distance b_0. The parameter σ_0 will allow us to adjust the wheelbase of the vortex

$$\omega(x, y, 0) = \frac{\Gamma_0}{\pi\sigma_0^2} \exp\Big(- \frac{(x - 0.5b_0)^2 + y^2}{\sigma_0^2} \Big) - \frac{\Gamma_0}{\pi\sigma_0^2} \exp\Big(- \frac{(x + 0.5b_0)^2 + y^2}{\sigma_0^2} \Big) \qquad (3.1)$$

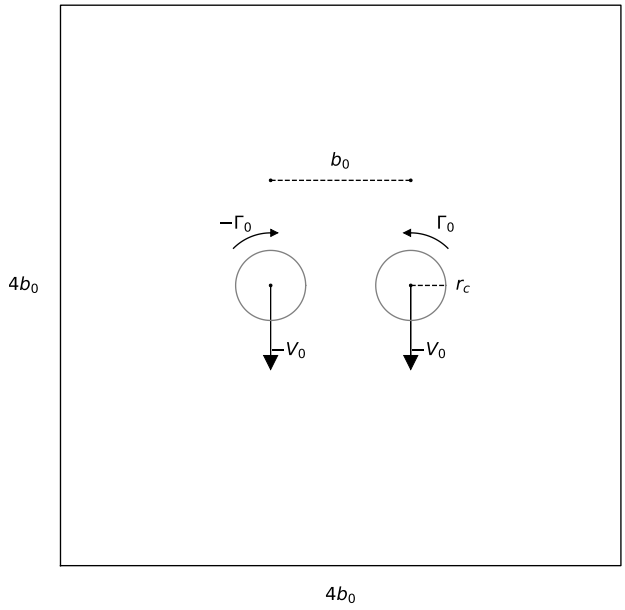

Figure 3.1: *Case representation : Two vortices of opposite circulation in a periodic box.*

The initial velocity field induced by a Gaussian vortex is

$$U_\theta(r) = \frac{\Gamma_0}{2\pi r}\Big(1 - \exp\big(-\frac{r^2}{\sigma_0^2}\big)\Big)$$

The maximum velocity of a Gaussian vortex is reached at $r_c = \sqrt{\beta\sigma_0^2}$ where $\beta = 1.2564$ is found numerically. As previously mentioned, the velocity support is infinite, meaning each vortex generates a downwash velocity that affects the other. The sum of the velocity induced by both vortices is called V_{ind}. Let V_0 be the velocity induced by a vortex at distance b_0, as it is the distance between both vortices, defined as

$$V_0 = U_\theta(b_0) = \frac{\Gamma_0}{2\pi b_0}\Big(1 - \exp\big(-\frac{b_0^2}{\sigma_0^2}\big)\Big) \approx \frac{\Gamma_0}{2\pi b_0}$$

The last approximation is valid when $b_0 >> \sigma_0$, this is the case for two vortices that have no interaction between each other.

As mentioned in the introduction, the case studied here is a rough approximation of the wake vortices generated by an aircraft. Of course, the simulation take place in 2D, so there is no turbulence and thus no wake simulation. Note also that Gaussian vortex used here are not the best approximation for wake vortices, LOA (Low Order Algebraic) vortex, also called Burnham-Hallock vortex, or HOA (High Order Algebraic) vortex seem to be a better representation, [5]. The last hypothesis is that in real life, we have a larger domain (almost infinite) but here we consider a periodic box. If the box length L, is large compared to the case studied, it seems to be a good approximation. Here we consider a box of $L = 4b_0$. Later in this section, we will

compare the V_0 obtained analytically for an infinite domain with the V_0 obtained in the periodic domain.

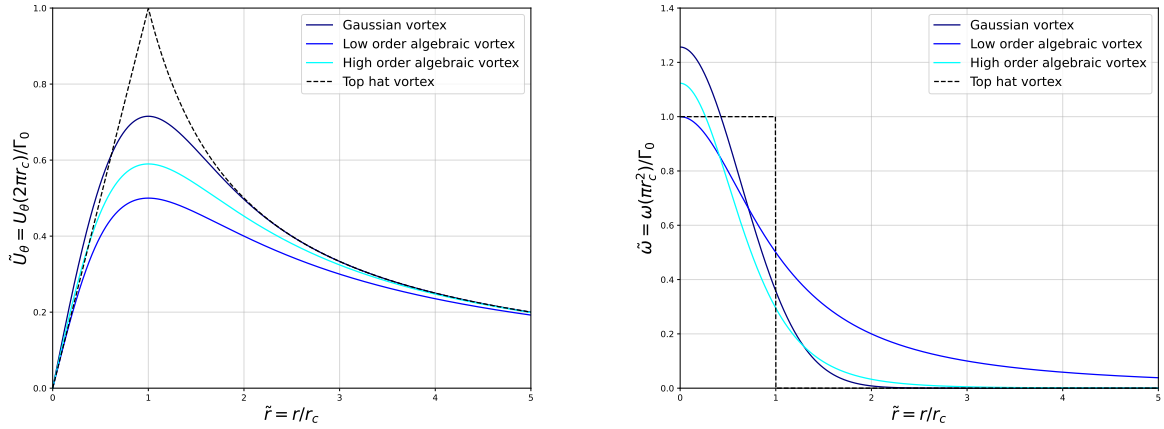

Figure 3.2: *Velocity and vorticity profiles of some vortex shape.*

To find the initial velocity condition, we use the vorticity-streamfunction formulation[1] as follows

$$\nabla^2 \psi = -\omega$$

$$\nabla \times \psi = u$$

It means that we solve a Poisson equation using $\omega(x, y, 0)$ and we can recover $u^0_{i,j} = \frac{\partial \psi}{\partial y}$ and $v^0_{i,j} = -\frac{\partial \psi}{\partial x}$, the initial discretized velocity field at the mesh point. This is the same as solving the Biot-Savart law to get the initial velocity. This Poisson equation is solved with a periodic boundary condition. We can then compare the analytical V_{ind} and the discrete value $v^0_{i,j}$ obtained numerically. As shown in Figure 3.3, V_{ind} is not exactly the same as in a periodic domain, especially far from the center. This is because other vortices are close to the limits of the computational box and they can interact as shown in Figure 3.4. We can observe that the velocity at the center of the vortices ($\tilde{x} = 0.5$ and $\tilde{x} = -0.5$) is quite similar for both cases. This velocity is not negative (not zero) and so the dipole is advected downwards. The larger the domain size L is, the better the approximation of the periodic domain will be. The profile obtained has the same shape as the wake generated by an airplane. We have a zone where we get an upwash velocity, this is called the "sweet spot" and can be used in formation flying to save fuel [29], and we have a zone between the two vortices where we get a downwash velocity.

[1] A complete vorticity-streamfunction solver using a collocated grid on a non-uniform resolution has also been developed for this master's thesis, few papers that help are [27, 28]. It will not be used except for this first step to recall the initial velocity profile based on the vorticity condition.

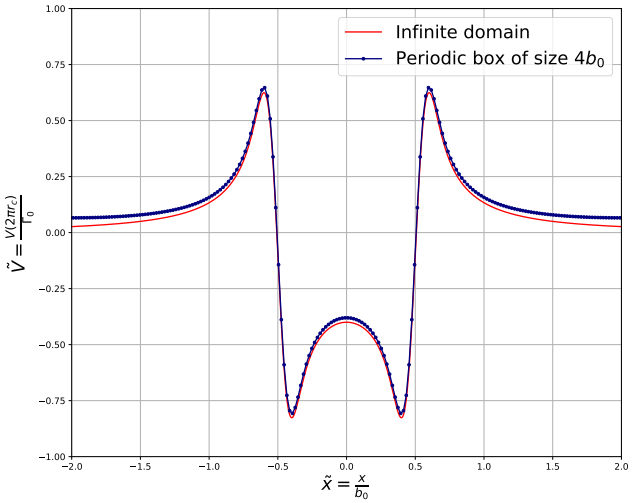

Figure 3.3: *Initial velocity profile $\tilde{V}(\tilde{x}, \tilde{y} = 0)$, theoretical result in an infinite domain and the simulated result for a periodic domain of size $L = 4b_0$.*

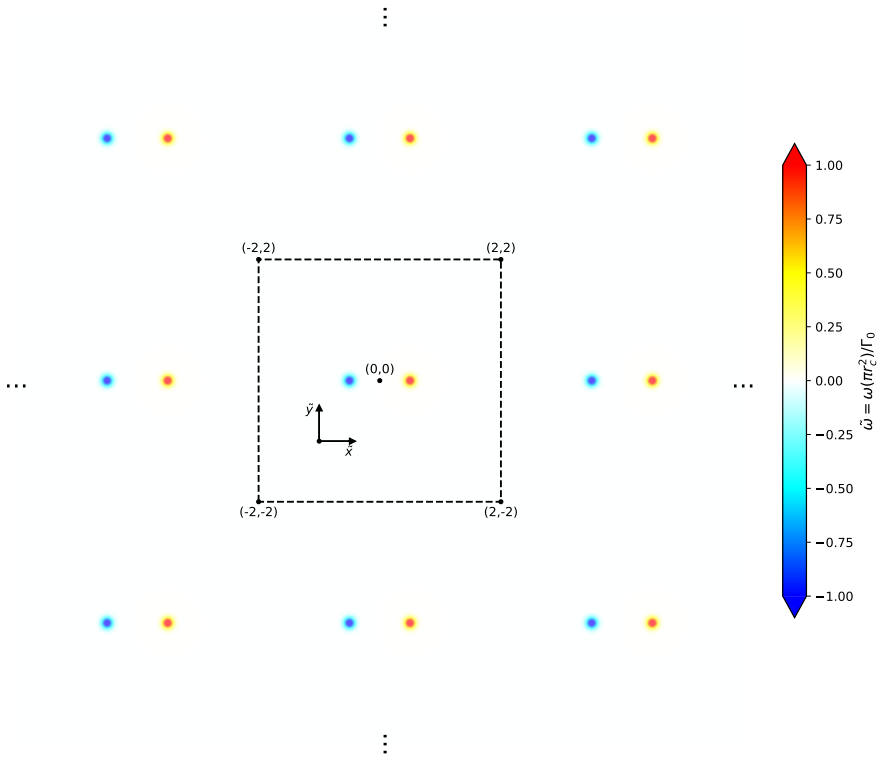

Figure 3.4: *Representation of the periodic case in the dimensionless plane $(\tilde{x} = \frac{x}{b_0}, \tilde{y} = \frac{y}{b_0})$.*

The case can be completely defined by dimensionless ratios. A dimensional number, called the Reynolds number and defined by $Re_\Gamma = \frac{\Gamma_0}{\nu}$, represents the ratio between inertial and viscous effects. A length ratio that represents the radius of the maximum velocity of a vortex over the length between the two vortices, $\frac{r_c}{b_0}$. If this ratio is small, it means that the vortices are far from each other and that the box length $L = 4b_0$ is large compared to the vortex size (better approximation of the infinite domain). If the ratio is larger than 0.5, the interactions between the vortices are significant because the vortices are close to each other. The space discretization is linked to the case thought the ratio $\frac{h}{\sigma_0}$, generally we say that when ratio $\frac{h}{\sigma_0}$ is bigger than 0.5, the Gaussian vortex is not correctly resolved. The timestep of the integration scheme is obtained by forcing a value for the Courant-Friedrich-Levy number, $CFL = \frac{U_{max}\Delta t}{h}$ where $U_{max} = U_\theta(r_c)$.

The basic case we will analyze corresponds to dimensionless numbers:

- $Re_\Gamma = \frac{\Gamma_0}{\nu} = 10000$
- $\frac{r_c}{b_0} = 0.1$
- $\frac{h}{\sigma_0} = 0.226$
- $\frac{L}{b_0} = 4$
- $CFL = 0.1$

Note that $\frac{h}{\sigma_0} = 0.226$ allows us to have an integer number of points to cut the grid. The number of points is $m = n = 198$. This number must be divisible by 2 and 3 to allow the mapping function to run properly.

3.2 Analysis of the uniform results

In the uniform case, we see that the dipole is advected with its induced downwash velocity and diffused in time, as shown in Figure 3.5. The vortex is advected along a vertical direction. We can compare the time $\tilde{t} = 0$ with the time 5.08. In both cases the dipole is in the center of the box at the same position, but in the latter case the vortices are more diffused, so the maximum point is lower and the spread is larger. The diffusion term will be analyzed in more detail in the next section. We can also observe that there is no visible interaction between the left and right vortices at this ratio $\frac{r_c}{b_0}$. Note that in this figure and all the others, gray dots represent 1 over 4 grid points, this will be the case throughout this thesis as plotting all points is a bit heavy and produces bad visual effects.

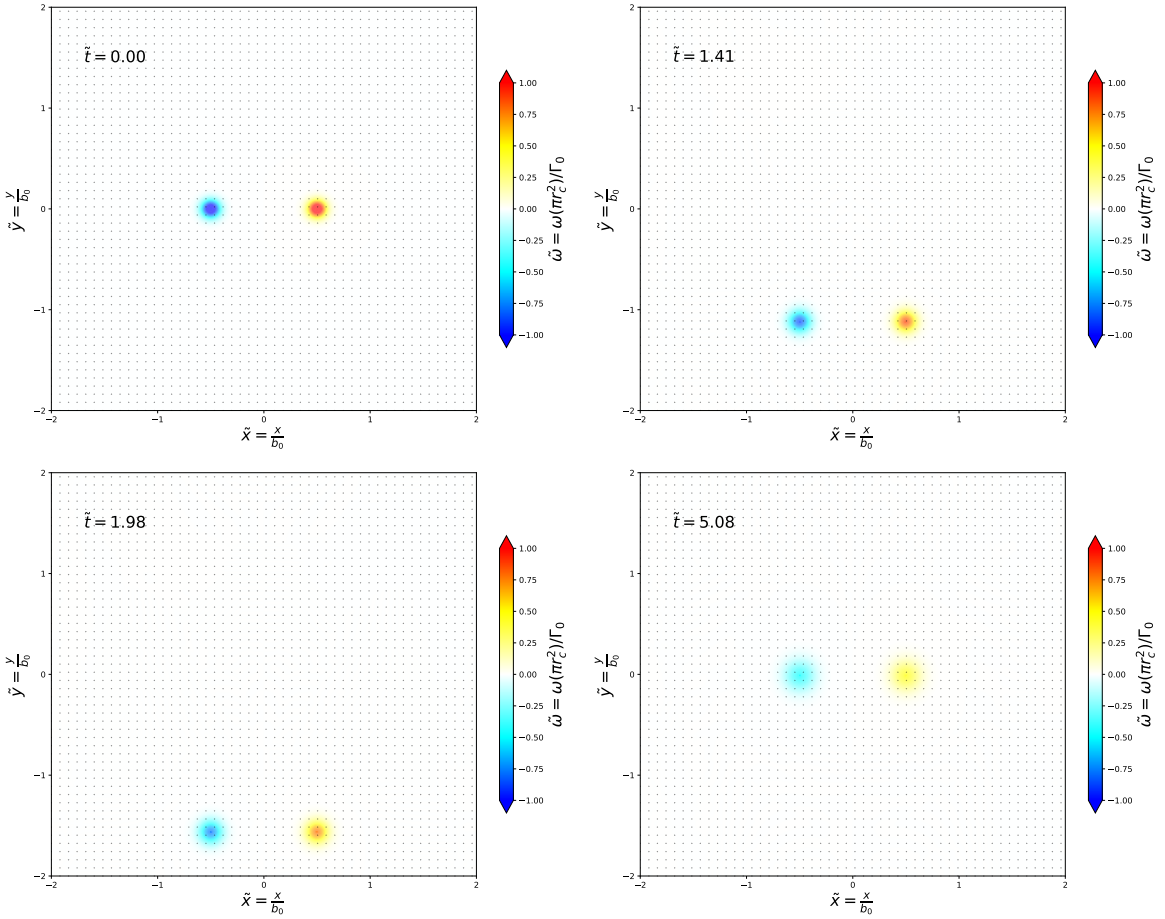

Figure 3.5: *Vorticity field of the dipole vortex in a periodic box at* $\tilde{t} = 0, 1.41, 1.98$ *and* 5.08*, for the case* $\frac{h}{\sigma_0} = 0.226$*. The light gray points correspond to the grid points, every fourth point is drawn.*

We can analyze the spatial order of the uniform solver, it should be of order 2 since all the finite differences used are of order 2. We study the convergence of the 2- and ∞-norms of the error. Given the reference field, the dimensionless errors are defined as

$$E_2 = \frac{(\pi r_c^2)}{\Gamma_0}\sqrt{\frac{1}{N^2}\sum_{i,j}(\omega_{i,j}^{ref} - \omega_{i,j})^2} \qquad E_\infty = \frac{(\pi r_c^2)}{\Gamma_0}\max_{i,j}|\omega_{i,j}^{ref} - \omega_{i,j}| \tag{3.2}$$

The associated local convergence rates are

$$r_2 = \frac{\log(E_2^k/E_2^{k+1})}{\log(h^k/h^{k+1})} \qquad r_\infty = \frac{\log(E_\infty^k/E_\infty^{k+1})}{\log(h^k/h^{k+1})}$$

The data are stored in Table 3.1 and plotted in Figure 3.6. This confirms that our uniform space discretization is of order 2.

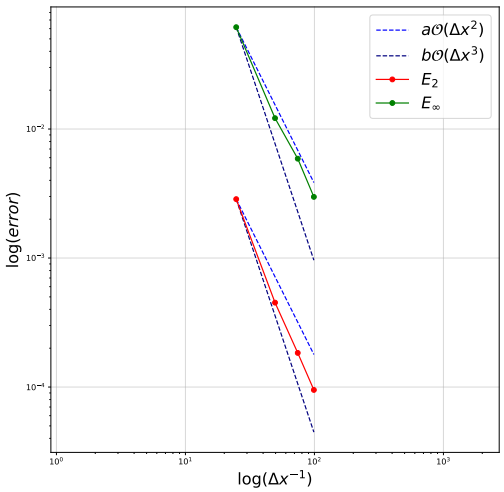

Figure 3.6: *Solver ∞-norm and 2-norm errors as a function of the discretization in the uniform case at dimensionless time $\tilde{t} = 1.41$. The reference used to compute the error is an overresolved simulation taken when $\frac{h}{\sigma_0} = 0.067$.*

N	h/σ_0	E_2	r_2	E_∞	r_∞
99	0.452	2.86e-03	/	6.16e-02	/
198	0.226	4.51e-04	2.67	1.21e-02	2.34
297	0.151	1.84e-04	2.21	5.89e-03	1.78
396	0.113	9.50e-05	2.30	2.98e-03	2.37

Table 3.1: *Table containing the errors and the local convergence rates at $\tilde{t} = 1.41$.*

In Figure 3.7 we see the pattern of the local error between $\frac{h}{\sigma_0} = 0.067$ and the cases $\frac{h}{\sigma_0} = [0.113, 0.151, 0.226, 0.452]$. In the coarsest case, the error is quite large, up to 5% of the maximum dimensional vorticity value. In general, we say that the Gaussian vortex is poorly resolved for $\frac{h}{\sigma_0}$ greater than 0.5, here we are close, so it is normal to have some error.

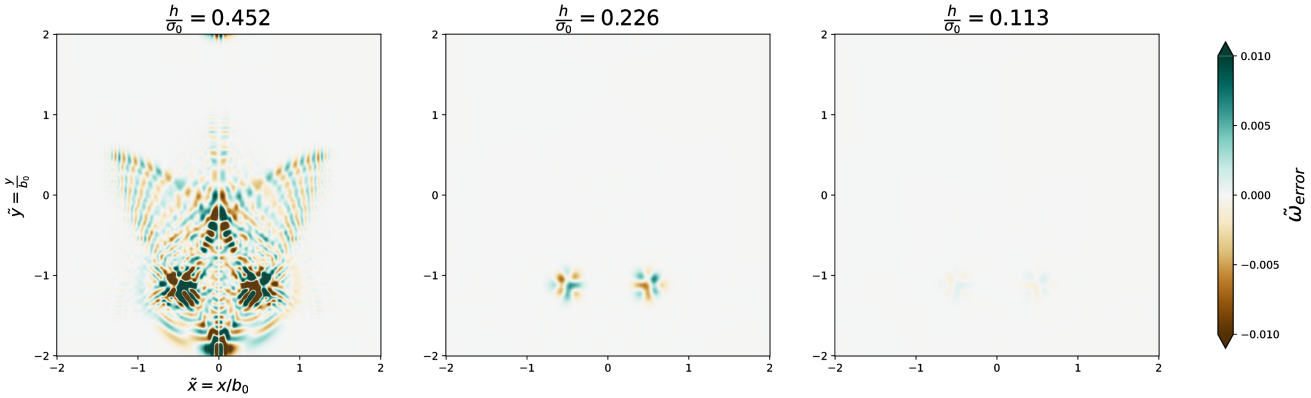

Figure 3.7: *Local error* ($\tilde{\omega}_{error} = \tilde{\omega}_{ref} - \tilde{\omega}$) *of the solver at time* $\tilde{t} = 1.41$*, the reference is a simulation taken at* $\frac{h}{\sigma_0} = 0.067$ *and the comparisons are done with* $\frac{h}{\sigma_0} = [0.452, 0.0226, 0.113]$ *going from left to right. The color plot is saturated at* 1% *of the dimensional vorticity* $\tilde{w}$*.*

We can modify the case and try with $\frac{r_c}{b_0} = 0.5$ so that the vortices are closer together. Obviously, this creates interactions between the two vortices. We can observe in Figure 3.8, the initial state and the interaction where a filament is generated and ejected upward. After a long time there will be only one Lamb-Chaplygin dipole left, which will diffuse with time [30, 31].

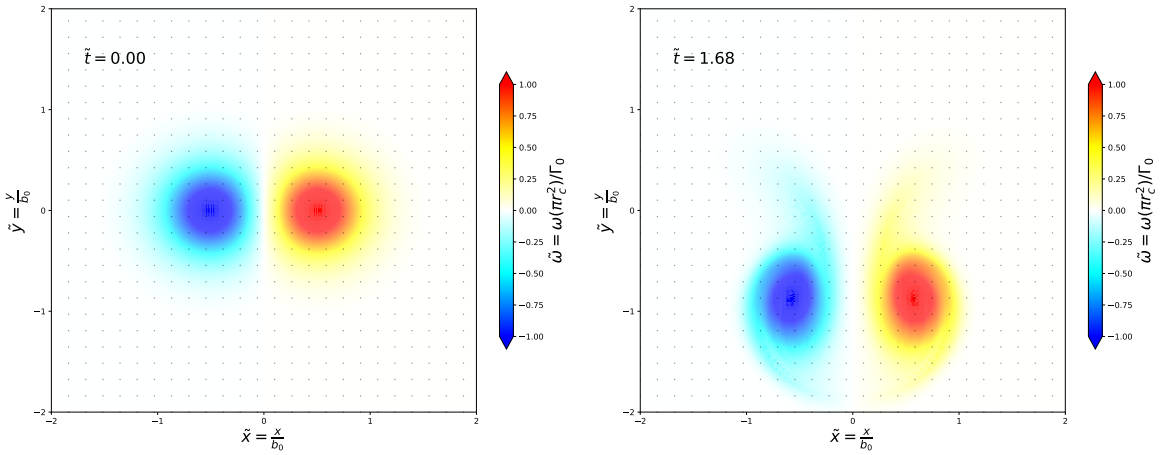

Figure 3.8: *Vorticity field of the dipole vortex in a periodic box at* $\tilde{t} = 0$ *and* 1.68*, for the case* $\frac{r_c}{b_0} = 0.5$ *and* $\frac{h}{\sigma_0} = 0.091$*. The light gray points correspond to the grid points, every fourth point is drawn.*

3.3 Verification of the diffusion term

In this section, we will compare our simulation results with the analytical form of the pure diffusion of a Gaussian function. Since we want to find the analytical solution of the diffusion, we will start the analysis with the 1D case and then derive the result for the 2D case. Let's start with a 1D Gaussian in a periodic domain of size L at time 0.

$$\omega(x,0) = \frac{\Gamma_0}{\pi\sigma_0^2}\exp\Big(-\frac{x^2}{\sigma_0^2}\Big)$$

Using the Fourier transform we can rewrite the initial Gaussian as a sum of modes.

$$\omega(x,0) = \sum_{j=-\infty}^{\infty}\hat{F}(k_j)\exp(ik_jx)$$

where

$$\hat{F}(k_j) = \frac{1}{L}\int_{L/2}^{L/2} f(x)\exp(-ik_jx)dx$$

where $k_j = \frac{2\pi j}{L}$ is the wavenumber. We will derive the analytical solution of the 1D diffusion equation

$$\frac{\partial\omega}{\partial t} = \nu\frac{\partial^2\omega}{\partial x^2}$$

This takes the form

$$\omega(x,t) = \sum_{j=-\infty}^{\infty}\hat{F}(k_j)\exp(ik_jx)\exp(-\nu k_j^2t)$$

Considering that in an unbounded domain we have

$$I = \int_{-\infty}^{\infty}\omega(x,0)dx = \frac{\Gamma_0}{\sqrt{\pi}\sigma_0}$$

The Fourier transform of a Gaussian is a Gaussian where each mode is given by

$$\hat{\omega}(k,0) = \frac{\Gamma_0}{\sqrt{\pi}\sigma_0 L}\exp\Big(-\frac{k^2\sigma_0^2}{4}\Big)$$

Consider a large periodic domain ($L >> \sigma_0$), approximation is better when $\frac{L}{\sigma_0}$ is large

$$\omega(x,0) \approx \frac{\Gamma_0}{\sqrt{\pi}\sigma_0 L}\sum_{j=-\infty}^{\infty}\exp\Big(-\frac{k_j^2\sigma_0^2}{4}\Big)\exp(ik_jx)$$

The evolution in time is thus

$$\begin{aligned}\omega(x,t) &\approx \frac{\Gamma_0}{\sqrt{\pi}\sigma_0 L}\sum_{j=-\infty}^{\infty}\exp\Big(-\frac{k_j^2\sigma_0^2}{4}\Big)\exp(ik_jx)\exp(-k_j^2\nu t)\\ &= \frac{\Gamma_0}{\sqrt{\pi}\sigma_0 L}\sum_{j=-\infty}^{\infty}\exp\Big(-\frac{k_j^2(\sigma_0^2+4\nu t)}{4}\Big)\exp(ik_jx)\end{aligned}$$

If we let $\sigma(t)^2 = \sigma_0^2 + 4\nu t$ and we take $\sigma(t) = \sigma_t$ to simplify the notation, we get

$$\omega(x,t) \approx \frac{\Gamma_0}{\sqrt{\pi}\sigma_t L}\frac{\sigma_t}{\sigma_0}\sum_{j=-\infty}^{\infty}\exp\Big(-\frac{k_j^2\sigma_t^2}{4}\Big)$$

Which is the initial condition that replaces σ_0 with σ_t and with a scaling factor of $\frac{\sigma_t}{\sigma_0}$

$$\omega(x,t) = \frac{\Gamma_0}{\pi\sigma_t^2}\frac{\sigma_t}{\sigma_0}\exp\Big(-\frac{x^2}{\sigma_t^2}\Big)$$

This means that the initial Gaussian, diffused over time, retains a Gaussian shape. We can now do the same analysis for the 2D Gaussian vortex [32] and we will get the Equation 3.3. We can see that the only change in the 2D case is that we do not have the scaling term $\frac{\sigma_t}{\sigma_0}$. This is due to the fact that the integral in an unbounded 2D domain considering the initial vortex no longer involves σ_0.

$$\omega(x,y,t) = \frac{\Gamma_0}{\pi\sigma_t^2}\exp\Big(-\frac{x^2+y^2}{\sigma_t^2}\Big) \tag{3.3}$$

Note that the only important relation is

$$\frac{\sigma_t^2}{\sigma_0^2} = 1 + 4\nu t = 1 + 4\frac{\sqrt{\beta}}{Re_\Gamma}\frac{\Gamma_0}{V_0}\frac{b_0}{r_c}\tilde{t}$$

where $\tilde{t} = \frac{tV_0}{b_0}$ is the dimensionless time. By superposing the solution of a diffusing vortex, we can find an analytical solution of the diffusion of the initial condition given by Equation 3.1. We can then compare it with the result of our two vortices in a periodic box, this is shown in Figure 3.9.

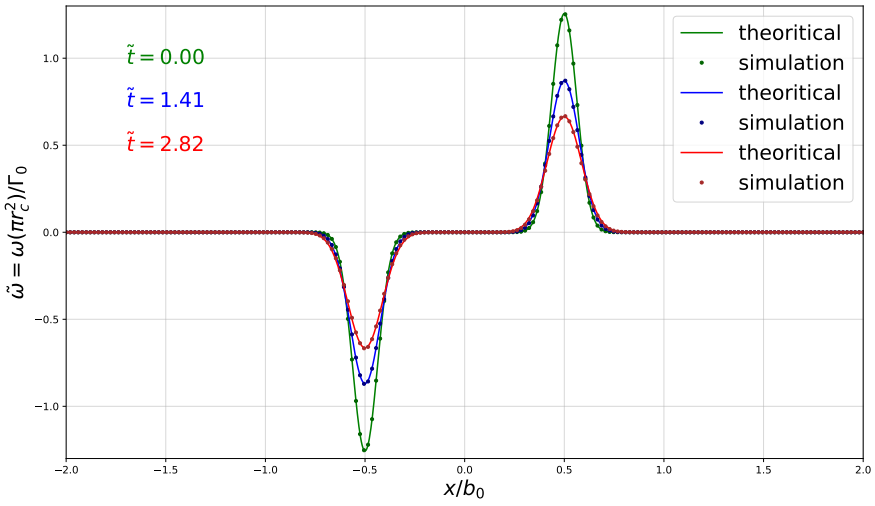

Figure 3.9: *Comparison of the dimensionless vorticity between the analytical result of the 2D Gaussian vortex diffusion (lines) and the simulation with* $\frac{h}{\sigma_0} = 0.226$ *(dots).*

3.4 Analysis of the non-uniform results

After the uniform case, we will now study the non-uniform case. We will start with the vortex dipole in a zone where we have a uniform discretization. Then we want to progressively coarsen the grid in the direction of the vortex convection, i.e. in the y direction. The desired non-uniform discretization is constructed using a mapping function $y = g(\eta)$.

First, let's introduce some notations, $\Delta(x)$ is the non-uniform space step size and is denoted Δ for simplicity and h is the space step size in the uniform region. We will compare two cases, each starting in an area where the resolution is uniform where $\Delta = h$. Then we will have a zone where the resolution will be non-uniform. In the first case, we will go from $\Delta = h$ to $\Delta = 2h$, so a two times coarser zone. In the second case, we will go from $\Delta = h$ to $\Delta = 4h$, so a 4 times coarser zone. Mappings are found by part, we have the central zone where the mapping is uniform between $\eta = 1.5$ and 2.5. The other two zones are represented by polynomials of degree 5. Their 6 coefficients are determined by ensuring continuity, as well as the continuity of the first and second derivatives. The mapping function and its derivative are shown in the Figure 3.10. We observe that $g_2'(\eta)$ increases from 0.5 to 2, indicating a change of 4 in the discretization. Similarly, $g_1'(\eta)$ increases from $\frac{1}{3}$ to $\frac{2}{3}$, signifying a change of 2 in the discretization. We can see that the polynomial is of the first mapping is non-monotonic, we will keep it anyway, as we want to see if the mitigation model developed further in thesis will care about this.

$$g_1(\eta) = \begin{cases} 0.1317\eta^5 - 0.3951\eta^4 + 0.1975\eta^3 + 1.3333\eta & \text{, if } \eta \leq 1.5 \\ \frac{(2\eta+2)}{3} & \text{, if } 1.5 < \eta < 2.5 \\ 0.1317\eta^5 - 2.2387\eta^4 + 14.9465\eta^3 - 48.7243\eta^2 + 78.2387\eta - 47.6872 & \text{, if } 2.5 \leq \eta \end{cases}$$

$$g_2(\eta) = \begin{cases} -0.0988\eta^5 + 0.5926\eta^4 - 1.0370\eta^3 + 2\eta; & \text{, if } \eta \leq 1.5 \\ \frac{(\eta+2)}{2} & \text{, if } 1.5 < \eta < 2.5 \\ -0.0988\eta^5 + 1.3827\eta^4 - 7.3580\eta^3 + 18.7654\eta^2 - 22.4938\eta + 11.8025 & \text{, if } 2.5 \leq \eta \end{cases}$$

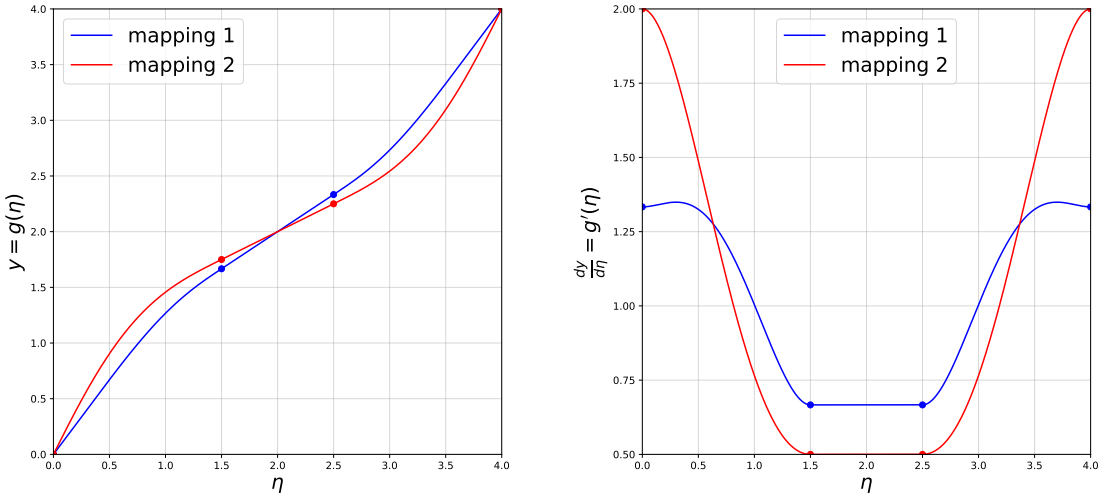

Figure 3.10: *Illustration of the mapping functions and their derivatives used for the two Gaussian vortices in a periodic box. Mapping 1 shows a coarsening by a factor of* 2*, while mapping 2 shows a coarsening by a factor of* 4*.*

Using the first mapping, we see that the vortices are correctly convected, as shown in Figure 3.11. They are follow the correct trajectories. In the right plots, where the color map is saturated at 0.1 of the dimensional vorticity, we can observe the dispersion error resulting from the non-uniformity of the resolution. This error trails behind the vortex, pointing toward the center of the system as the vortex progresses. The maximum value of the error is close to a dimensionless vorticity of 0.05.

Using the second non-uniform mesh, we see in Figure 3.12 that the error takes the same form as with mapping 1 but is more pronounced. This is because the vortices reach a value of $\frac{\Delta}{\sigma_0} = 0.904$ in the coarsest region. The beginning of the error is created when the vortex reaches a value where $\frac{\Delta}{\sigma_0} > 0.35$. It can be observed that the error is of the order of the center point of the vortex. If we solve the same case with $\frac{h}{\sigma_0} = 0.112$ instead of 0.224, the error is more moderate.

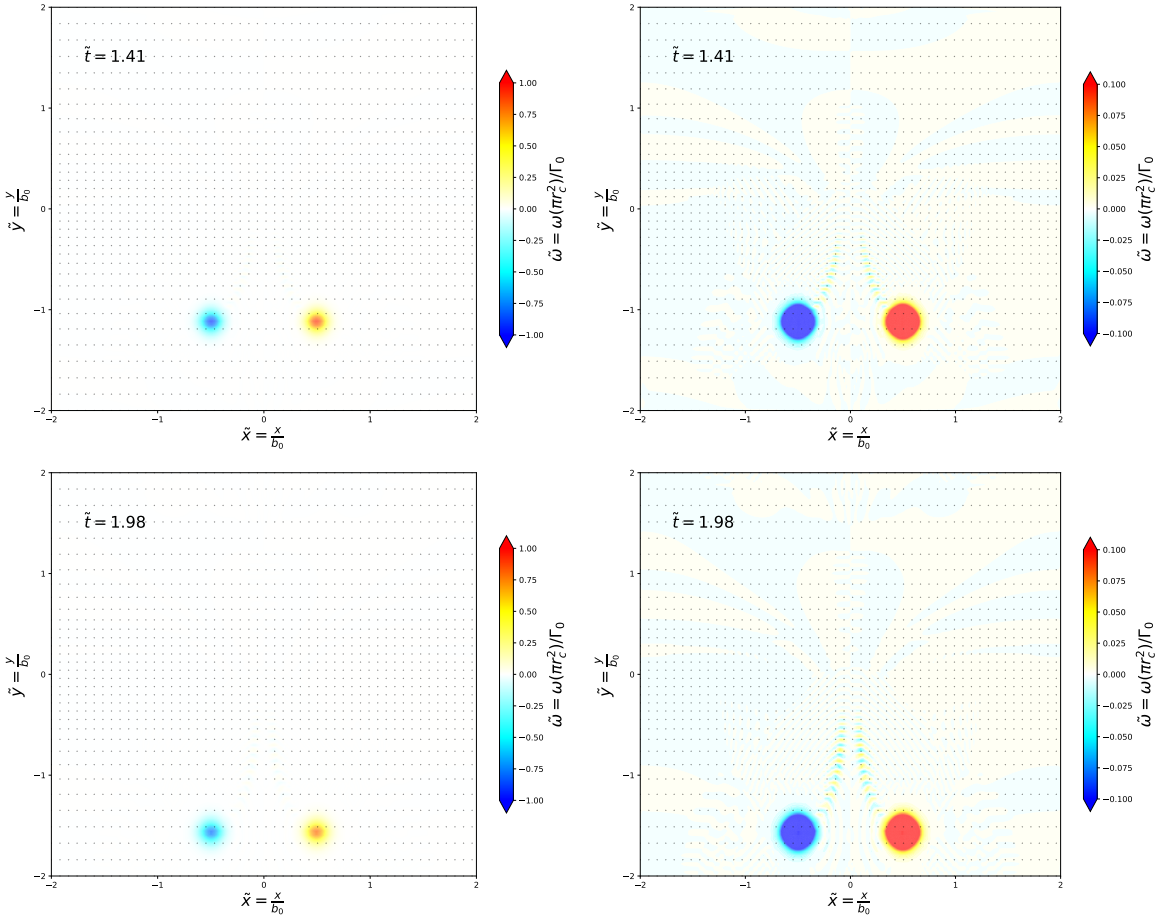

Figure 3.11: *Vorticity plot of the vortex dipole at time* $\tilde{t} = 1.41$ *and* 1.98 *with a non-uniform grid using mapping* 1*. Each plot on the left is the result of the dimensionless vorticity* $\tilde{w}$*. The corresponding plots on the right are the same, but with a saturated color plot for* $|\tilde{w}| > 0.1$*.*

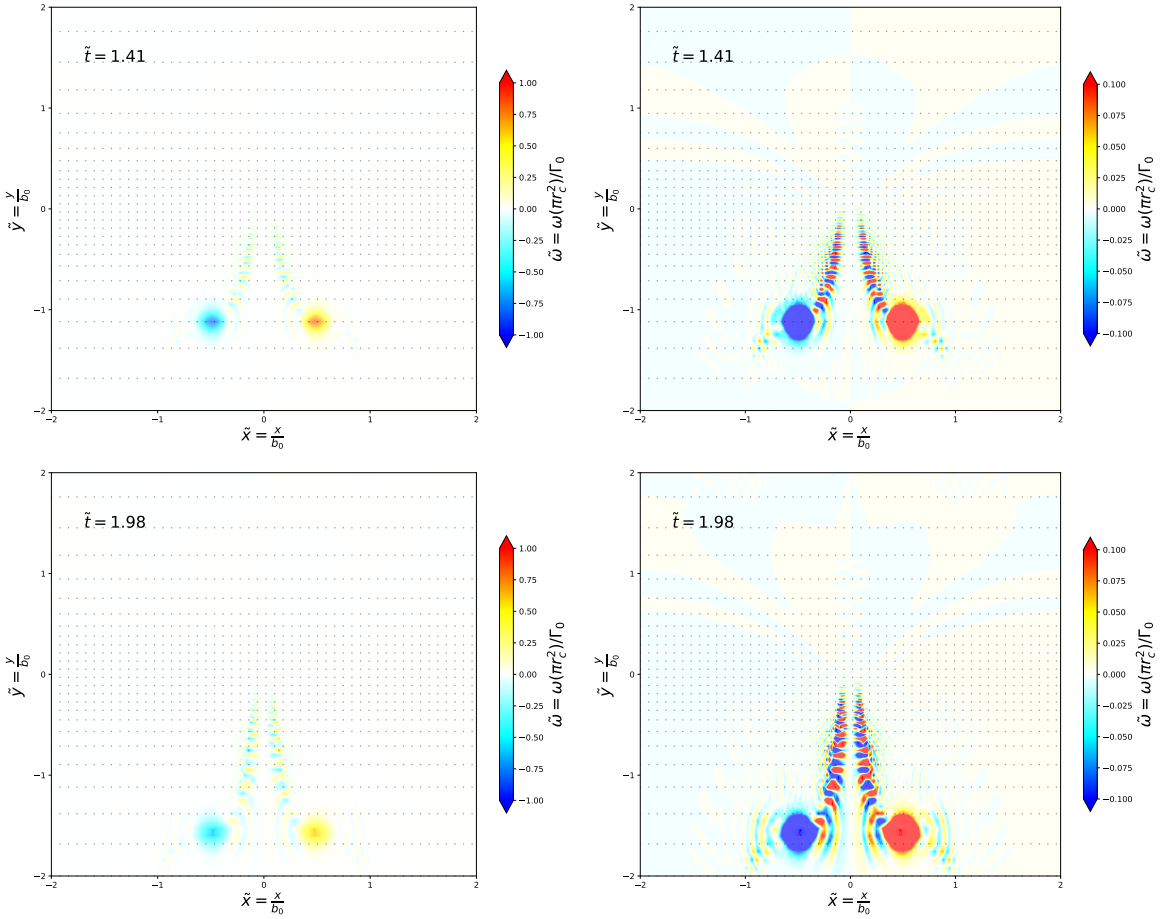

Figure 3.12: *Vorticity plot of the vortex dipole at time* $\tilde{t} = 1.41$ *and* 1.98 *with a non-uniform grid using mapping* 2*. Each plot on the left is the result of the dimensionless vorticity* $\tilde{w}$*. The corresponding plots on the right are the same, but with a saturated color plot for* $|\tilde{w}| > 0.1$*.*

We can observe the trajectories of the local extremum value of each vortex to discern if the non-uniformity of the mesh causes a deviation in the vortex direction. This is shown in Figure 3.13. The correct direction is the vertical line. With the first mapping function, the vortex is almost perfectly convected. For the second mapping, the maximum point of the vortex deviates from the straight trajectories. Then the maximum point is no longer in the center of the vortex, it is located in the error generated by the passing vortex. This proves that the errors are of the same order of magnitude as the case.

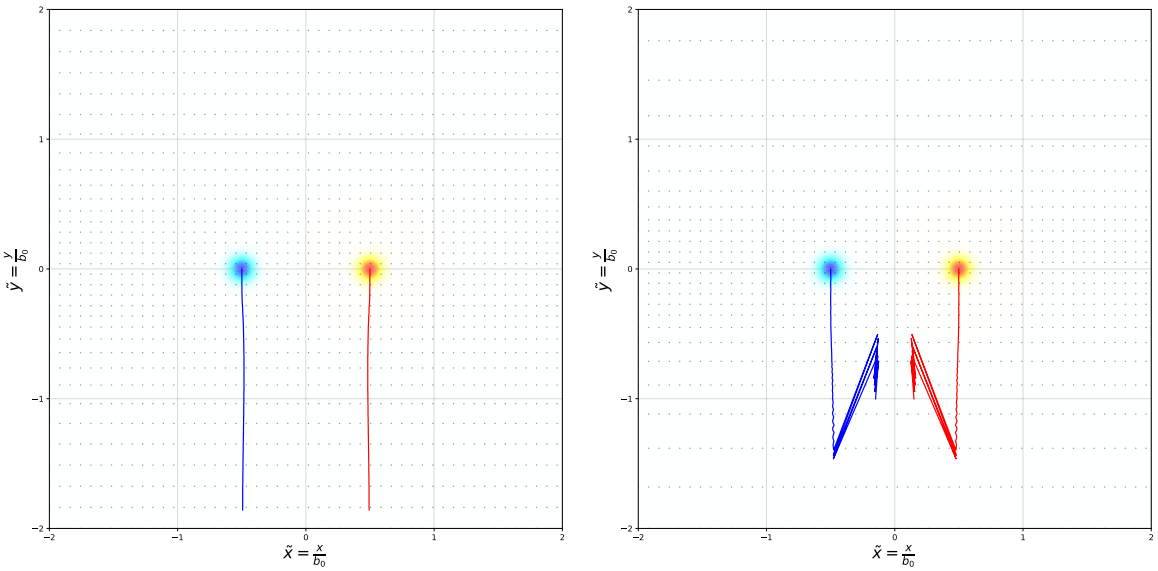

Figure 3.13: *Tracer of the position of the local extremum value of each vortex for the dimensional time between* $\tilde{t} = [0, 2.26]$*, on the left using mapping 1 and on the right using mapping 2.*

Note that a good way to validate all the indices of the space discretization is to run the same simulation, but oriented in the other directions. The code should give the same result, which is what it does here. In this way, we make sure that the indices are correct. This validation technique was also used in the Poiseuille case developed in the previous chapter.

3.5 Case variation : Angle of incidence with the mesh

Now we want to create the same case but with the vortex induced velocity that has an angle of attack with the non-uniform resolution called α. We want to do this to see if the error pattern is still the same. A representation of the situation is shown below in the Figure 3.14.

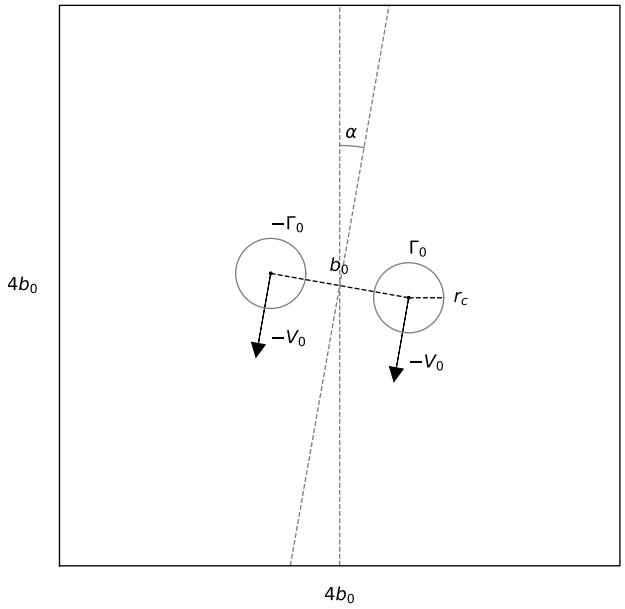

Figure 3.14: *Case representation with an angle of attack α between the mapping in y direction and the induced velocity of the two vortices.*

We have performed the simulation with an angle of attack of $\alpha = 10°$ and the second mapping function, $g_2(\eta)$. This is shown in Figure 3.15. The errors still take the same form as with $\alpha = 0$, i.e. some oscillation in the wake of the vortex. Note that the dispersion errors generated by each vortex are no longer symmetric. In Figure 3.16, we have shown the trajectories of the absolute maximum point of each vortex. We can see that the vortices are deviated from their initial trajectories and that the maximum points are on the left part instead of being symmetric with the trajectories.

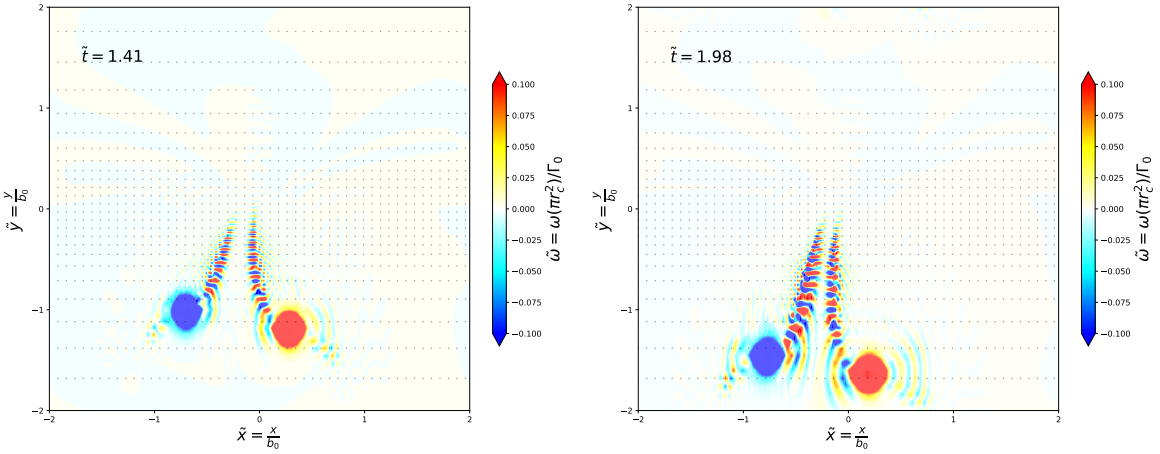

Figure 3.15: *Vorticity plot of the vortex dipole at time* $\tilde{t} = 1.41$ *and* 1.98 *with a non-uniform grid using mapping* 2*. The dipole vortex is tilted at an angle of* 10 *with respect to the horizontal. The color plot is saturated for* $|\tilde{w}| > 0.1$*.*

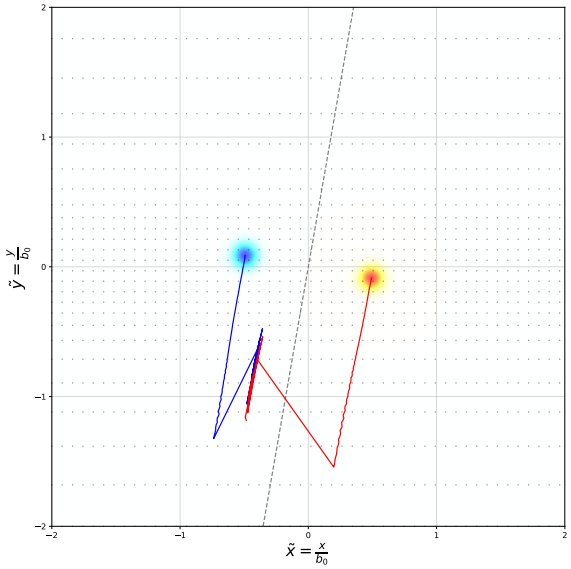

Figure 3.16: *Tracer of the position of the local extremum value of each vortex for the dimensional time between* $\tilde{t} = [0, 2.26]$ *using mapping 2. The dipole vortex is tilted at an angle of* 10° *with respect to the horizontal.*

Chapter 4

Mitigation of the error due to non-uniform mesh resolution

In this chapter, we want to reduce the dispersion error we get when coarsening a resolution. We will base our work on the paper "Effects of resolution inhomogeneity in large-eddy simulation" from Yalla et al., [9], which tries to mitigate the commutation error in the Large Eddy Simulation (LES). The commutation error is caused by the inability of the non-uniform filter and the derivative operator to commute, which is often ignored in practice [33]. The paper proposed a term to mitigate this error. The goal of this chapter is to investigate whether the model proposed in their paper could work for the dispersion errors obtained in a Direct Numerical Simulation (DNS) with variable resolution. We will rewrite their proposed model in a more classical form and try to understand in detail how it works. We will then apply it to the case developed in the previous chapter.

4.1 Introduction to the mitigation model

The mitigation model proposed in the paper [9] tries to mitigate commutation error in non-uniform filtering LES simulation. The filtered Navier-Stokes momentum equations is given by Equation 4.2 where the filter is represented by $\bar{\cdot}$.

$$\overline{\frac{\partial u_i}{\partial x_i}} = 0 \tag{4.1}$$

$$\frac{\partial \overline{u}_i}{\partial t} + \overline{\frac{\partial u_i u_j}{\partial x_j}} = -\overline{\frac{\partial p}{\partial x_i}} + \nu \overline{\frac{\partial^2 u_i}{\partial x_j \partial x_j}} \tag{4.2}$$

The commutation error, written $\mathcal{C}(u)$ and defined by 4.3, occurs when we commute the derivative operator with the non-uniform filtering operator. This error is derived and shown in [34] for a smooth filter example. Note that ∂ is used for the actual operator and δ is used for the discrete operator. Similar to $\mathcal{C}(u)$, we can define $\mathcal{C}^2(u)$ as the commutator operator for the viscous term.

$$\mathcal{C}(u) = \overline{\frac{\partial u}{\partial x}} - \frac{\delta \overline{u}}{\delta x} \tag{4.3}$$

Following this and introducing the subfilter scale stress τ_{ij}^{SFS} defined as $\tau_{ij}^{SFS} = \overline{u}_i\overline{u}_j - \overline{u_i u_j}$. The discretized form of 4.2 can be written as [33]

$$\frac{\delta \overline{u_i}}{\delta x_i} = 0 \tag{4.4}$$

$$\frac{\partial \overline{u}_i}{\partial t} + \frac{\delta \overline{u}_i \overline{u}_j}{\delta x_j} = -\frac{\delta \overline{p}}{\delta x_i} + \nu \frac{\delta^2 \overline{u}_i}{\delta x_j \delta x_j} + \frac{\delta \tau_{ij}^{SFS}}{\delta x_j} - \mathcal{C}(u_i u_j) - \mathcal{C}(p) + \nu \mathcal{C}^2(u_i) \tag{4.5}$$

Most commonly, all $\mathcal{C}$ terms are neglected and only the subfilter scale stress is modeled. Commutation terms are often ignored because they are complex to represent. In LES, we focus more on the type of filter, the location of the cutoff frequency in the spectrum and the choice of the subgrid scale stress model [35]. We model the subgrid scale stress τ_{ij}^{SGS} to represent the effect of small and unresolved scales where the kinetic energy is dissipated as heat on the resolved scale. This can be done using the Smagorinsky model [36] or the RVM model [37, 38]. The latter is a high-pass filtered turbulent viscosity model.

Which subgrid scale stress model is the best? Which low-pass filter is better, box, Gaussian, sharp cutoff? What percentage of the turbulence spectrum do we want to resolve? These questions are the first priority in LES. They are still open questions, even though a lot of work has been done on them [39]. Here we will focus on the commutation errors. These errors would be negligible for the viscous term and even more when Re is high. The commutation errors of the pressure term can be subsumed in the modified pressure when we ensure the continuity equation. The convective term is often the most important term in many problems, so the commutation error associated will be less negligible. Therefore, in the paper that interested us [9], they propose a model for this term. The convective term can be rewritten in the advective form, so the problem is reduced to modeling $u_j\mathcal{C}(u_i)$. After statistical and series analysis of the error, they came up with a model. Note that the proposed term is developed based on the part of the error resulting from non-uniformity and not for the part resulting from the numerical error arising from the discretization of the term. The model follows

$$\mathcal{C}(u) \approx (-1)^{N/2} C \Delta \frac{d\Delta}{dx}\Big(\Delta^{N-2} F_N(\overline{u})\Big) \tag{4.6}$$

$$C = \frac{(-1)^{(N-2)/2}\log(\epsilon)}{2(\frac{\Delta_c - \Delta_f}{\Delta_c})\Delta^N \hat{F}_N(\kappa_{max})} \tag{4.7}$$

where $\delta = \delta(x)$ is the non-uniform space discretization, N is the order of the model, $F_N(u)$ is the term we want to model, it will approximate a high order derivative of order N, κ_{max} is the value at which the spectrum of the numerical model F will be maximum, ϵ is an arbitrary coefficient representing a tolerance level indicating the target fraction of incident energy that will

be reflected, and Δ_c and Δ_f represent the coarsest and finest spatial discretizations, respectively.

We can observe that the model $F_N(u)$ is an approximation of the high order derivative term of order N. This is sometimes called hyperdiffusion. In the next section, we will try to mitigate the dispersion error caused by a 1D convection using a hyperdiffusion term of order 4 and compare it to a classical diffusion. We can note that $\mathcal{C}(u)$ depends on $\Delta(x) = \Delta$, the variable space step size. It also depends on the local variation of the space step size $\frac{d\Delta}{dx}$, which means that the mitigation term is null when the resolution is uniform.

4.2 Further analysis of hyperdiffusion

What we are looking for here is the attenuation of the oscillations generated by the dispersion error. The goal is to use a high order derivative term, also called hyperdiffusion, to attenuate the dispersion error.

Here we will introduce the effect of hyperdiffusion of order 4 on the dispersion error with a 1D case in uniform resolution. The case considered will be two Gaussian functions, one centered in $x = 0.25$m characterized by $\sigma_1 = 0.025$m and the other in $x = 0.75$m characterized by $\sigma_2 = 0.0125$m in a periodic 1D domain of length $L = 1$m. The initial condition is given by Equation 4.8, note that the quantity u is considered as a dimensionless quantity. We consider a convection where the dispersion errors are mitigated by a diffusion term and a convection where the errors are mitigated by a hyperdiffusion term of order 4. The corresponding partial derivative equation is given by Equation 4.9. Note that the hyperdiffusion term requires a minus sign to be stable when the hyperdiffusion coefficient α is considered positive.

$$u_0 = \exp\left(-\frac{(x-0.25)^2}{\sigma_1^2}\right) + \exp\left(-\frac{(x-0.75)^2}{\sigma_2^2}\right) \tag{4.8}$$

$$\frac{\partial u}{\partial t} + c\frac{\partial u}{\partial x} = \nu\frac{\partial^2 u}{\partial x^2} - \alpha\frac{\partial^4 u}{\partial x^4} \tag{4.9}$$

The time integration is done with Runge-Kutta 4. All terms are discretized with second order central finite differences, the convection term will create dispersion as some modes are not properly convected. A modal analysis of the discrete convection term, as properly developed in Appendix B, gives us that the mode k is convected with a modified velocity c^*.

$$c^* = c\left(\frac{\sin(kh)}{kh}\right)$$

where h is the space step size.

We compare three cases : a pure convection ($c = 1\text{ms}^{-1}$), a convection-diffusion ($c = 1\text{ms}^{-1}$ and $\nu = 2.2 \times 10^{-4}\text{m}^2\text{s}^{-1}$) and convection-hyperdiffusion ($c = 1\text{ms}^{-1}$ and $\alpha = 2.8 \times 10^{-8}\text{m}^4\text{s}^{-1}$). This is done for values of ν and α chosen to have the lowest 2-norm error, found by iteration. The results obtained are shown in Figure 4.1. The advantage of hyperdiffusion over standard diffusion relies on its ability to accentuate high frequency spreading while better preserving low frequencies from diffusion. In conventional diffusion, the peak of the Gaussian (small modes) is reduced from its initial state, which can lead to excessive error. Hyperdiffusion offers a compromise by reducing the diffusion of low frequencies while improving the diffusion of higher frequencies. However, it introduces a slight overshoot not observed in conventional diffusion, creating a negative bump on either side of the Gaussian. This behavior can be found in nature, for example in the spreading of waves in thin films or in the evaporation of water droplets. These phenomena are also represented by an equation involving a derivative of order 4, [40, 41].

We can notice that the 2-norm error based on the analytical solution over the whole domain, shown in the Table 4.1, is smaller for hyperdiffusion than for diffusion. This example was used to show how the hyperdiffusion term acts to reduce the oscillations compared to diffusion. There is a potential to explore and this will be done in the next section where we will apply the model developed in the previous section to your DNS with non-uniform resolution.

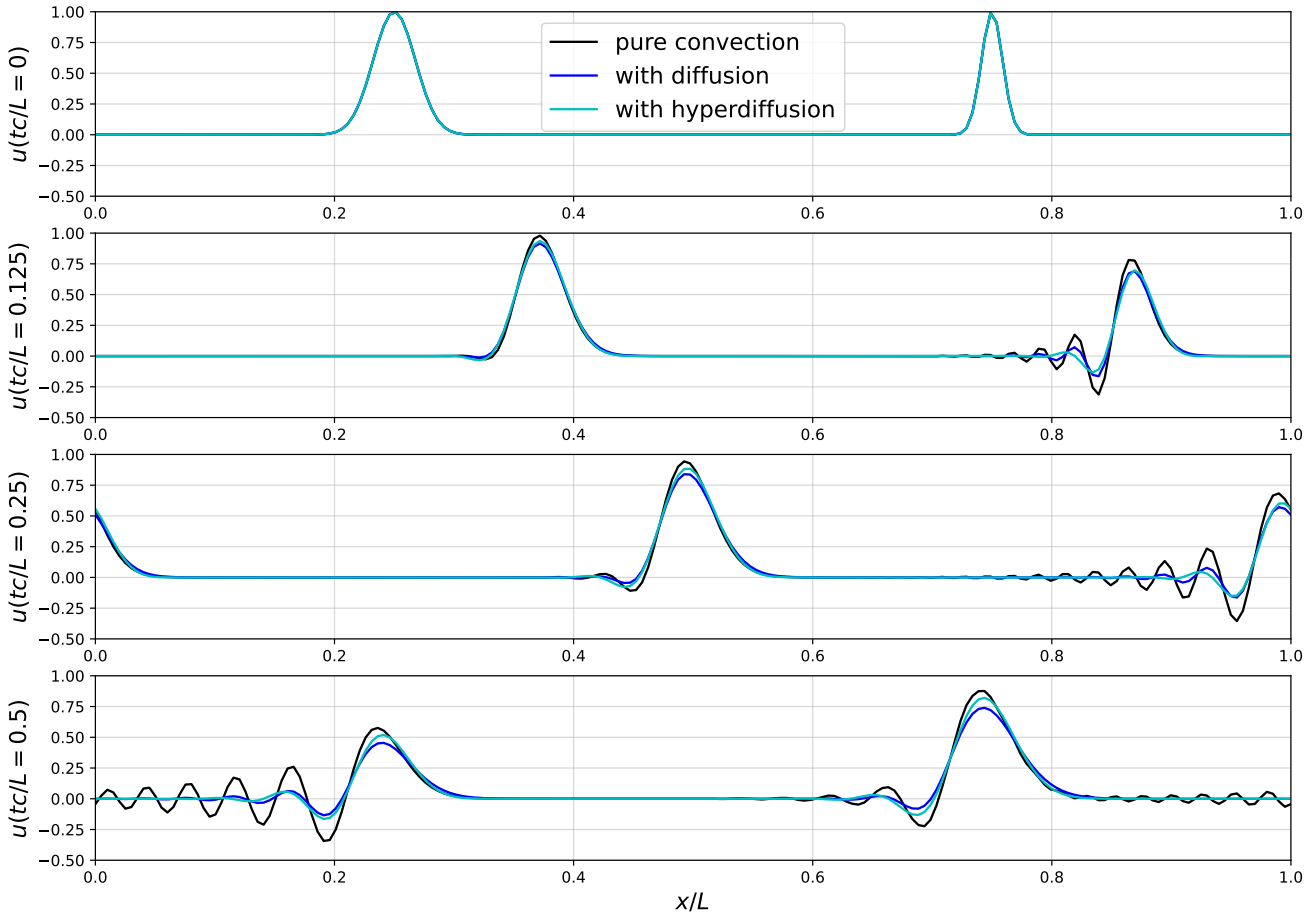

Figure 4.1: *Convection* ($c = 1\text{ms}^{-1}$) *of two Gaussians,* $\sigma_1 = 0.025\text{m}$ *for the left one and* $\sigma_2 = 0.0125\text{m}$ *for the right one. The space discretization is* $h = 0.005\text{m}$. *A pure convection and two cases where we try to mitigate the dispersion error, one with diffusion* $\nu = 2.2 \times 10^{-4}\text{m}^2\text{s}^{-1}$ *and one with hyperdiffusion* $\alpha = 2.8 \times 10^{-8}\text{m}^4\text{s}^{-1}$.

	convection	diffusion	hyperdiffusion
tc/L=0.125	0.0722	0.0607	0.0551
tc/L=0.25	0.1027	0.0861	0.0788
tc/L=0.5	0.1236	0.0967	0.0901

Table 4.1: *Table containing the 2-norm error for three cases : the pure convection, the convection-diffusion with* $\nu = 2.2 \times 10^{-4}\text{m}^2\text{s}^{-1}$ *and the convection-hyperdiffusion with* $\alpha = 2.8 \times 10^{-8}\text{m}^4\text{s}^{-1}$.

4.3 Application of the model to our DNS solver

Now, we would like to apply the model introduced in the first section of this chapter to our solver. In our case, we are working on DNS simulation, so we have no filter and we do not have the commutation error as in LES, we only have dispersion and diffusion errors. Our goal here is to verify if the model proposed in [9] can mitigate the dispersion error of the convection term obtained with the non-uniform resolution. Note that we will not correct the diffusion error here. Since the error is generated as high frequency, we can expect that the hyperdiffusion term proposed in the paper will correctly achieve its job of mitigation.

The model applied to our code will correspond to the case $N = 4$ and thus to

$$\mathcal{C}(u) \approx C\Delta \frac{d\Delta}{dx}\Big(\Delta^2 F_4(u)\Big)$$

The parameter C will be chosen experimentally to work well, it must obviously be related to the coarse space resolution Δ_c and the finest Δ_f. In the original paper, they used a function, developed Equation 4.7, but they still considered the parameter ϵ as an experimentally chosen tolerance, so in the end they also choose C experimentally.

To model the term $F_4(u)$ by a term close to the fourth derivative operator and to find its discretization, we will show the idea found by [9]. We will take the difference between the second derivative operator (CD_2) and the repetitive application of the first derivative operator (CD_1CD_1). Note that CD_x is a notation that represents the second order centered finite difference of the xth derivative. The advantage of this formulation is that for numerically well resolved wavenumbers (small modes) the operators cancel. However, for poorly resolved wavenumbers (higher modes), their difference is non-zero and can be used to filter out higher wavenumbers, as shown in Figure 4.2. The detailed calculation of the modified wavenumber is given in the second part of the appendix B. In essence, the operator acts as a filter for high wavenumbers. A small development in the uniform case, where h is the space step size, can prove that the operator corresponds to the fourth order derivatives up to a factor. It is important to note that in the original paper [9], the authors did not write this operator correctly, the development below is the correction and this can be verified using the application [42] which gives the coefficient for the different finite difference schemes.

$$\begin{aligned}
(CD_2 - CD_1CD_1)u_i &= \frac{u_{i+1} - 2u_i + u_{i-1}}{h^2} - \frac{u_{i+2} - 2u_i + u_{i-2}}{4h^2} \\
&= \frac{-u_{i+2} + 4u_{i+1} - 6u_i + 4u_{i-1} - u_{i-2}}{4h^2} \\
&= -\frac{h^2}{4}\frac{\delta^4 u}{\delta x^4}\Big|_i \\
&\approx -h^2 F_4(u_i)
\end{aligned}$$

We will reproduce this method in the code to find the discretization of the term on the non-uniform resolution. The complete discretization is presented in Appendix C.

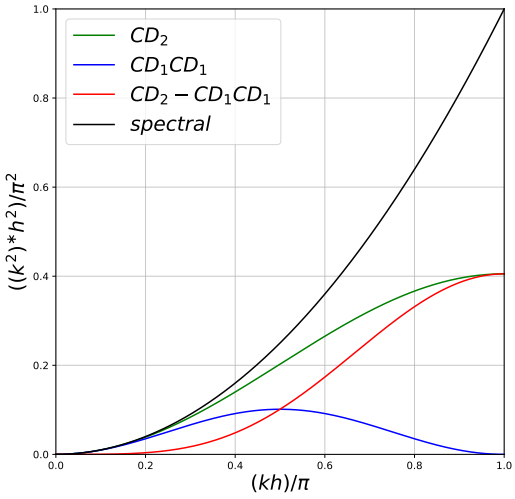

Figure 4.2: *Modified wavenumber of* (CD_1CD_1) *and* (CD_2) *scheme compared to the perfect wavenumber (spectral). We also show the difference* $(CD_2 - CD_1CD_1)$.

4.4 Analysis of the mitigation model results

In this section, we apply the mitigation term for $N = 4$, using the discretization $(CD_2 - CD_1CD_1)u$ to model $-\Delta^2 F_4(u)$, to the case : two Gaussian vortices in a periodic box.

For the first mapping, we see in Figure 4.3 that the error is well corrected. The errors almost disappear and reach values $< 0.1\%$ of the dimensionless vorticity instead of $< 0.5\%$. The best value of C, after several tries, seems to be around 1.5.

For the second mapping, the error is more pronounced as seen in Figure 4.4. With the mitigation term we can observe that some of the dispersion error is mitigated. The error is no longer of the order of the vortex dimensionless vorticity. The error is still large but reduced. $C = 1$ seems to be a good compromise between mitigation and instability. A different value of C can be taken, if C is too small we observe less effect of the mitigation term. If C is taken bigger, the dispersion is more attenuated but instabilities are generated at the front of the vortex. A more detailed comparison of different values is shown below. Note that here we mitigate the dispersion error but we do not correct the vortex shape error or the diffusion error, as shown in the satured Figure 4.5.

We can observe that the best value of the coefficient for mapping 1 and mapping 2, seems to follow the proportionality $C \propto \frac{\Delta_c}{\Delta_c - \Delta_f}$ introduced in the model of the coefficient that paper [9] proposed.

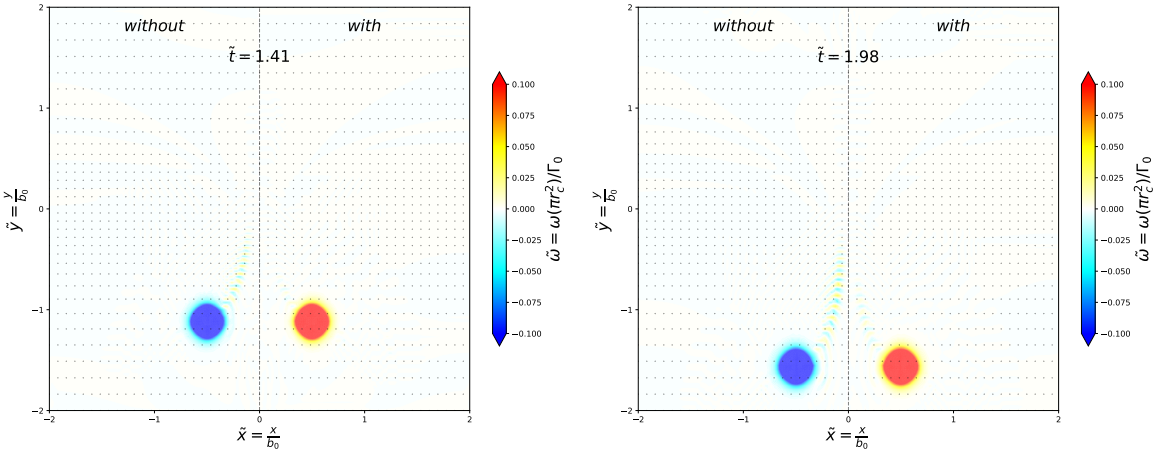

Figure 4.3: *Comparison of the dimensionless vorticity $\tilde{w}$ between case without and with mitigation term ($C = 1.5$) going from $\frac{\Delta}{\sigma_0} = 0.226$ to $\frac{\Delta}{\sigma_0} = 0.452$. The color plot is saturated for $|\tilde{\omega}| > 0.1$.*

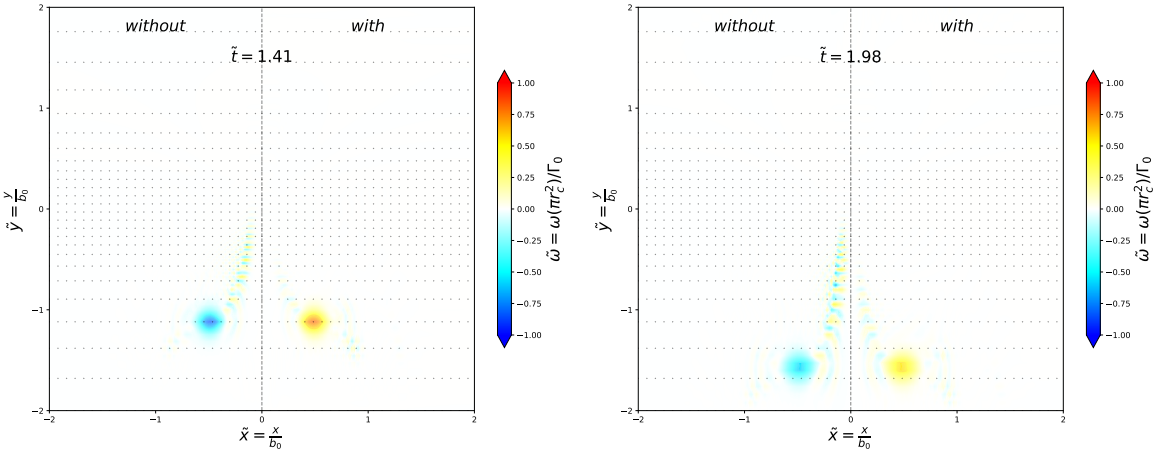

Figure 4.4: *Comparison of the dimensionless vorticity $\tilde{w}$ between case without and with mitigation term ($C = 1$) going from $\frac{\Delta}{\sigma_0} = 0.226$ to $\frac{\Delta}{\sigma_0} = 0.904$. The color plot is saturated for $|\tilde{\omega}| > 1$.*

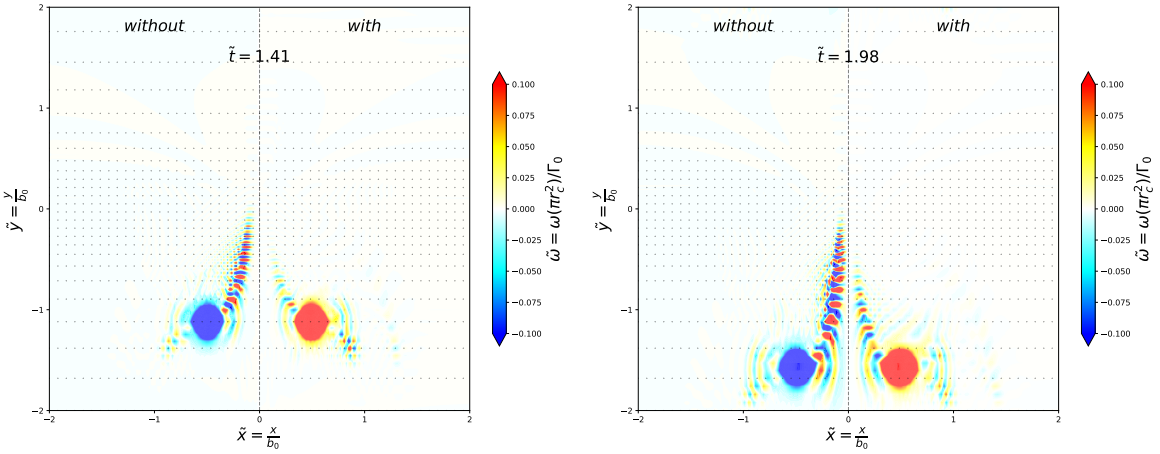

Figure 4.5: *Comparison of the dimensionless vorticity $\tilde{w}$ between case without and with mitigation term ($C = 1$) going from $\frac{\Delta}{\sigma_0} = 0.226$ to $\frac{\Delta}{\sigma_0} = 0.904$. The color plot is saturated for $|\tilde{\omega}| > 0.1$.*

Tracing the trajectories of the extremum value of each vortex confirms that the error is no longer of the order of the case for mapping 2, we can compare the initial result without mitigation Figure 3.13 with the result with the mitigation term Figure 4.6. The trajectory always follows the center of the vortex instead of being in the dispersion error of the vortex.

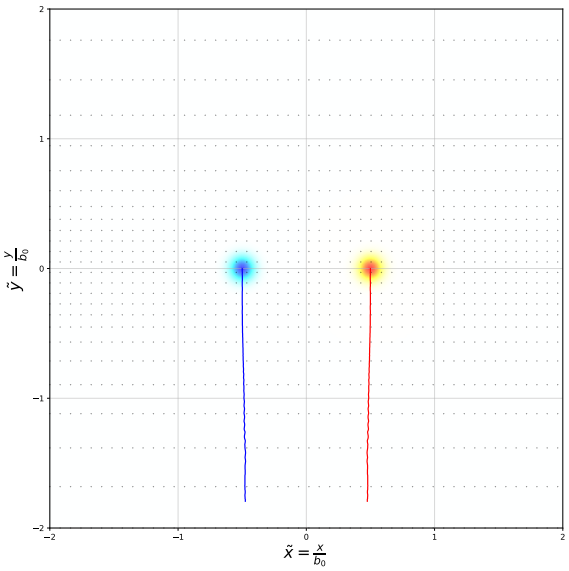

Figure 4.6: *Tracer of the position of the local extremum value of each vortex for the dimensional time between $\tilde{t} = [0, 2.26]$. The simulation is done on using mapping 2 with the mitigation term ($C = 1$).*

We can analyze the evolution over time of the 2- and ∞-norm errors computed with 3.2 for different values of the coefficient $C = [0, 0.5, 1, 1.5]$. This is shown in Figure 4.7. Note that $C = 0$ is the case with no damping term. We observe that before the dimensionless time $\tilde{t} \approx 0.5$, the dipole vortex moves in the region where the mesh is uniform, resulting in an error that is close to zero. After that, the discretization becomes coarse and errors start to be generated, the mitigation strategy starts to correct the error by applying hyperdiffusion. This reduces the maximum error value, in other words the ∞-norm error, E_∞. The error was of the order of the case (about 0.5 of the dimensionless vorticity), and when using the model with $C = 0.5$ and $C = 1$ the maximum error is divided by a factor of 2. The total error also decreases when viewed in the 2-norm error plot (E_2). However, if the parameter C is set too high, e.g. $C = 1.5$, hyperdiffusion will attenuate more the dispersion errors, but the mitigation term will inadvertently create new errors around the vortex, especially at the front and sides, which will increase the global errors instead of reducing them, as shown in Figure 4.8. This error increase is due to 2 reasons: the model discretization error and the excessive hyperdiffusion.

Without the mitigation model ($C = 0$), we observe that the error naturally decreases with time after the coarsening is finished $\tilde{t} \approx 2.5$, as the diffusion term performs its intended function, but also on the dispersion error. It can be considered as an autocorrection of the case. If the Reynolds number (Re_Γ) were higher or in an inviscid flow, this natural error cancellation would not occur, leaving the mitigation model as the only corrective mechanism. In the refinement zone starting after $\tilde{t} \approx 2.5$, the mitigation model leads to an increase in error rather than a correction. When the vortex re-enters the uniform mesh zone, the error stabilizes. If we let the vortex go again in the non-uniform zone, around time $\tilde{t} > 5$, since the vortex is more diffuse and better resolved, it will cause less dispersion error and it will lead to an overactive mitigation model due to its constant value of C.

This observation suggests that a variable coefficient over time might be more effective in this case. Since the vortex undergoes similar coarsening starting at $\tilde{t} = 0$ and $\tilde{t} = 5$, and the errors increase after $\tilde{t} = 5$ considering the same C. This means that the mitigation model also depends on the case analyzed and not just on the mapping function used. This will be explored in the next chapter, where the complexity of the simulated case will be increased.

For our specific case considering the passage over a distance corresponding to the periodic box size $L = 4b_0$, the optimal value of C appears to be $C = 1$.

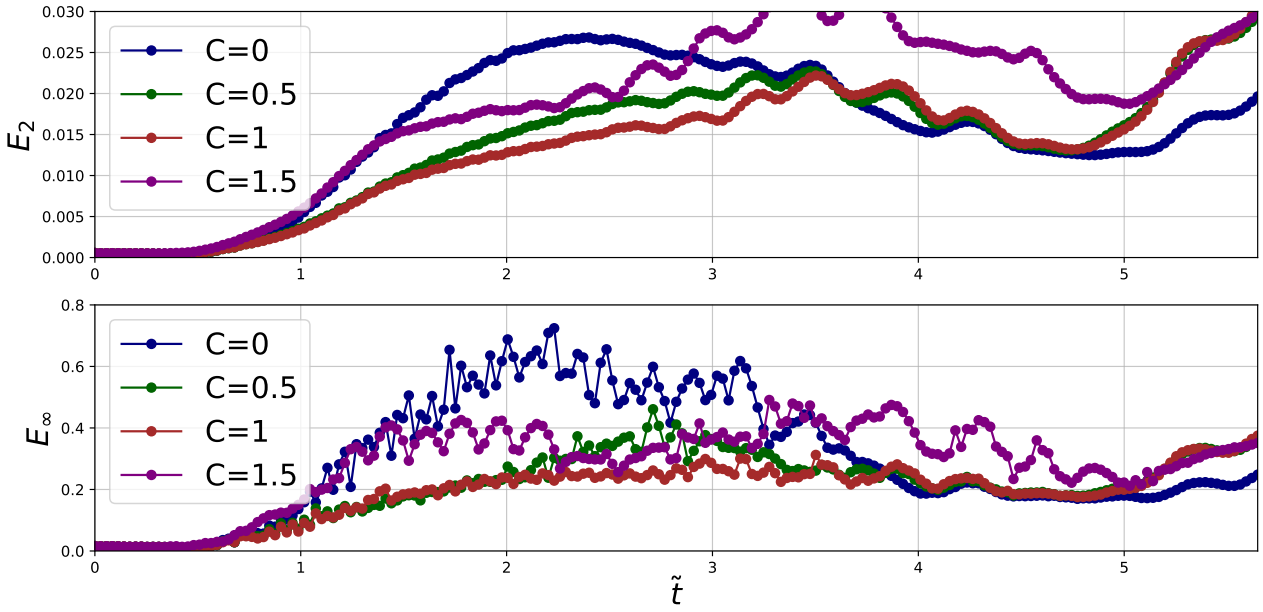

Figure 4.7: *Error plots (E_2 and E_∞) as a function of the dimensionless time $\tilde{t}$ comparing the mitigation model ($CD_2 - CD_1CD_1$) for different values of C. When the value of C is set to 0 it means that there is no mitigation.*

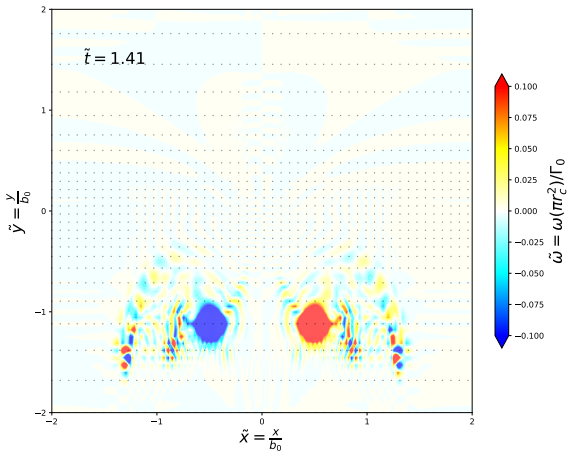

Figure 4.8: *Vorticity plot of the vortex dipole at time $\tilde{t} = 1.41$ with a non-uniform grid using mapping 2 and a mitigation term with $C = 1.5$. The color plot is saturated for $|\tilde{w}| > 0.1$.*

4.5 Analysis when increasing the order of the mitigation model

In this section, we will try to apply the $F_N(u)$ model but for $N = 6$ to see if we can get better results.

$$\mathcal{C}(u) \approx -C\Delta\frac{d\Delta}{dx}\big(\Delta^4 F_6(u)\big)$$

To model the term $F_6(u)$, we will apply three times the second order derivative. A development in the uniform case, where h is the space step size, shows us that applying three times the centered second order finite difference of the second derivative, called (CD_2), gives us the centered second order finite difference for the 6th derivative,

$$(CD_2^3)u_i = \frac{u_{i+3} - 6u_{i+2} + 15u_{i+1} - 20u_i + 15u_{i-1} - 6u_{i-2} + u_{i-3}}{h^6} = \frac{\delta^6 u}{\delta x^6}\bigg|_i \approx F_6(u_i)$$

This model is denoted by (CD_2^3) and is developed in detail for the non-uniform resolution in Appendix C. The results of the error for the different values of $C = [0, 0.025, 0.05, 0.075, 0.1]$ are shown in Figure 4.9. We can see that the range of values for the coefficient C that we must consider to obtain accurate results must be one order lower than for the $(CD2 - CD_1CD_1)$ model. The value of $C = 0.075$ that seems to be the best one. We can notice that the mitigation is not better with the model (CD_2^3) than with the model $(CD_2 - CD_1CD_1)$. The errors seem to be even larger after a time $\tilde{t} = 3$. This may be because higher derivatives in the coarse zone are harder to approximate on a non-uniform mesh with second order finite differences, and thus quickly introduce more error than what they are expected to correct.

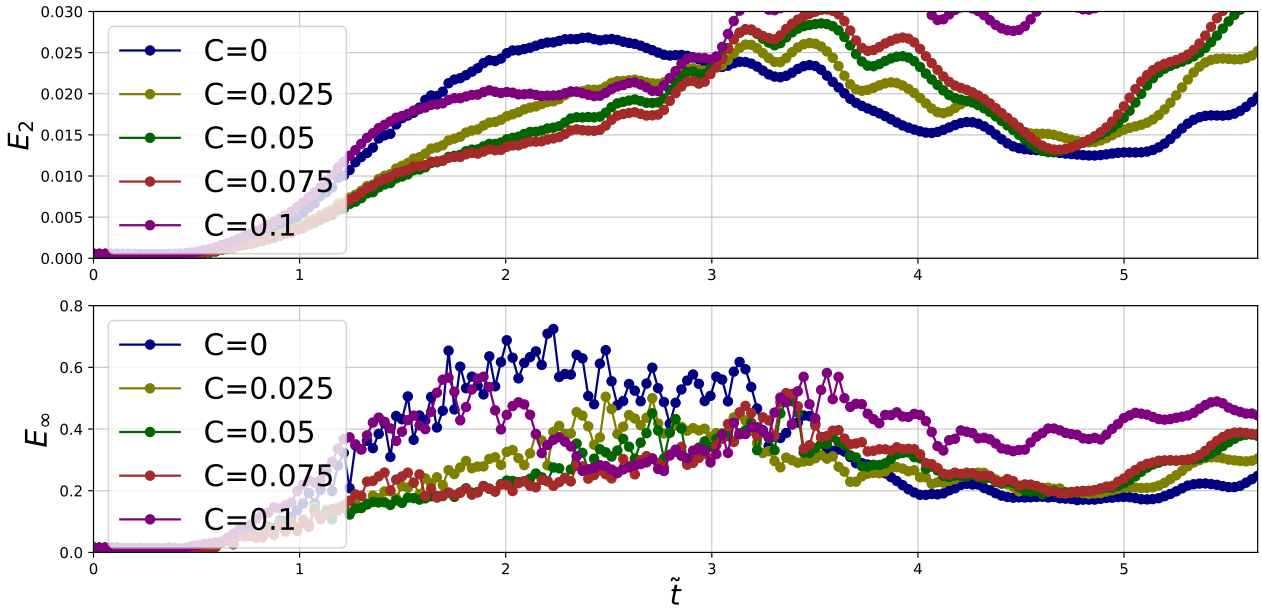

Figure 4.9: *Error plots (E_2 and E_∞) as a function of the dimensionless time $\tilde{t}$ comparing the mitigation model (CD_2^3) for different values of C. When the value of C is set to 0 it means that there is no mitigation.*

We can plot the modes treated by the derivative. We see in Figure 4.10 that the shapes are almost the same, but the low frequencies (small wavenumbers) are less diffused and more preserved when increasing the order of the hyperdiffusion. In practise, we can observe the dimensionless vorticity of the model for $C = 0.075$, in Figure 4.11. The mitigation model (CD_2^3) behaves like the model ($CD_2 - CD_1CD_1$) but new errors are added around the vortex, this show us visually that the model with $N = 6$ is not better than with $N = 4$. Note that as we increase the order of the attenuation term, we need to check that our timestep is still small enough, this can be done using a number equivalent to the Fourier number but for a higher order derivative term.

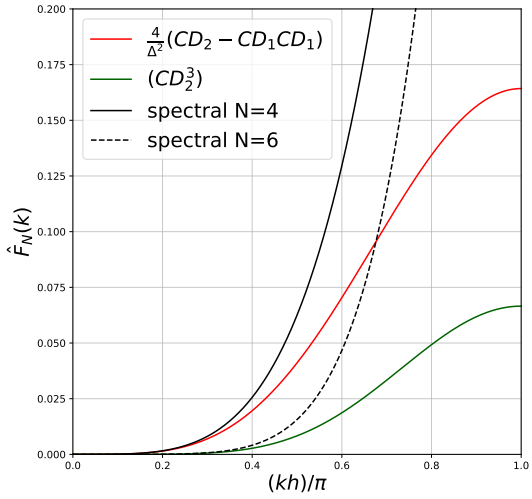

Figure 4.10: *Modified wavenumber of* $\frac{4}{\Delta^2}(CD_2 - CD_1CD_1)$ *and* (CD_2^3) *schemes compared to their respective derivative spectral curves.*

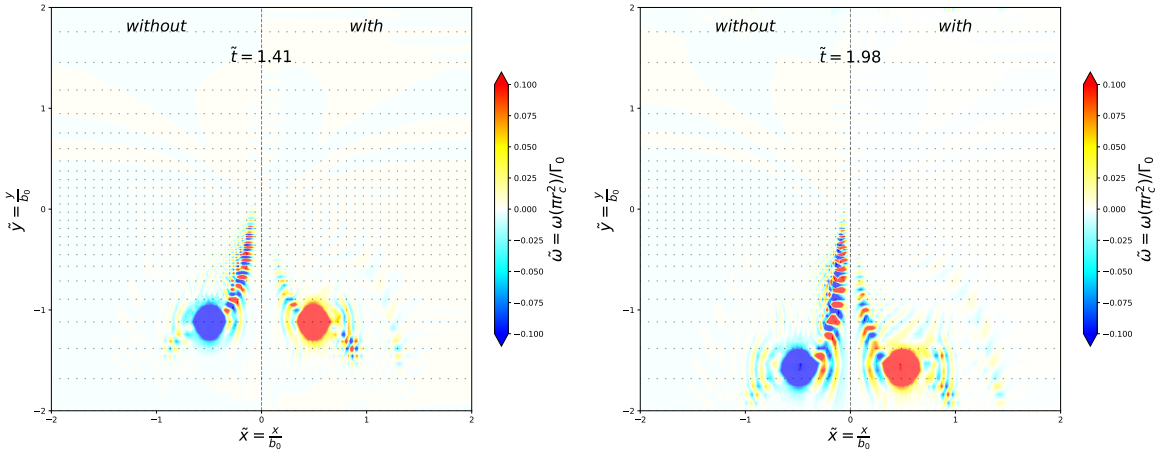

Figure 4.11: *Comparison of the dimensionless vorticity* $\tilde{w}$ *between case without and with mitigation model* (CD_2^3) *where* $(C = 0.075)$ *going from* $\frac{\Delta}{\sigma_0} = 0.226$ *to* $\frac{\Delta}{\sigma_0} = 0.904$. *The color plot is saturated for* $|\tilde{\omega}| > 0.1$.

Chapter 5

Four Gaussian vortices in a periodic box

In this chapter, we will apply the model to a more complex case. Finding a new case where the results can provide further understanding of the limitations of the mitigation model is not an easy task. We need a 2D case with some complexity that convects into a non-uniform mesh before diffusing all the small scales. In 2D turbulence, the cascade is not the same as in 3D, small scales are rapidly merged to create larger structure [43, 44]. Shedding of a flow past a complex geometry represented by a penalty method was an option as it can generate complex flow as analyzed in paper [45]. In order to generate a comparable results with the vortex dipole, we want to preserve the mapping functions used in the first case. That is why we choose a case that keeps the square periodic box. We will modify the case "Two Gaussian vortices in a periodic box" by adding two smaller Gaussian vortices to create a case called "Four Gaussian vortices in a periodic box". This case allows us to test two different behaviors with one geometry: one where the smaller vortex has the opposite sign of the larger one, and one where it has the same sign. We will be able to observe two completely different evolutions of the system just by changing the sign of the secondary vortices. The advantage of the two smaller vortices is that they create an interaction with the primary vortex and make the case more complex, so we will be able to test the mitigation model on two new cases that includes a wider range of scales [46].

5.1 Case presentation

In this first section we will introduce the case. The periodic box keeps the square shape of size L, where $\frac{L}{b_0} = 4$. The primary vortices are the same and located at the same place as in this two vortices case, $\frac{r_c}{b_0} = 0.1$. We will add two small Gaussian vortices of opposite circulation (called secondary vortices) in the center, in addition to the two primary vortices we had before. In doing so, we keep a zero circulation in the periodic box, since the two added primary vortices have a circulation of Γ_1 and $-\Gamma_1$. The two secondary vortices are separated by a length of b_1 and their radius is controlled by the parameter σ_1. The scheme of the situation is shown in Figure 5.1. Two cases will be examined: one where the secondary vortices rotate in opposite directions compared to the nearest primary vortex ($\Gamma_0 > 0$ and $\Gamma_1 > 0$), and one where they rotate in the same direction ($\Gamma_0 > 0$ and $\Gamma_1 < 0$).

These cases are defined using the following dimensionless ratios to connect the secondary vortex to the primary vortex:

- $\frac{b_1}{b_0} = 0.5$
- $\frac{\sigma_1}{\sigma_0} = 0.5$
- $\frac{\Gamma_1}{\Gamma_0} = \pm 0.25$

We first chose $\frac{b_1}{b_0}$ and $\frac{\sigma_1}{\sigma_0} = 0.5$, as we aim for secondary vortices with a radius 2 times smaller and that all vortices at the star are separated from the nearest by $0.25b_0$. Γ_1 is chosen so that the maximum absolute vorticity of each vortex is similar at time $\tilde{t} = 0$. As mentioned before, we keep the other ratios used to define the 2 vortex case. We will just change $\frac{h}{\sigma_0}$ and take a value of 0.113 instead of 0.226 to capture the smaller vortices. To get an idea of the resolution of the secondary vortices we need to consider the ratio $\frac{h}{\sigma_1}$, which will be 0.226. Note that additional vortices are placed at $(-0.5b_1, 0)$ and $(0.5b_1, 0)$. The case where $\Gamma_1 > 0$ is taken such that all vortices have signs that are altered, the initial vorticity condition is given by

$$\omega(x, y, 0) = \frac{\Gamma_0}{\pi\sigma_0^2} \exp\Big(- \frac{(x - 0.5b_0)^2 + y^2}{\sigma_0^2} \Big) - \frac{\Gamma_0}{\pi\sigma_0^2} \exp\Big(- \frac{(x + 0.5b_0)^2 + y^2}{\sigma_0^2} \Big) \tag{5.1}$$

$$- \frac{\Gamma_1}{\pi\sigma_1^2} \exp\Big(- \frac{(x - 0.5b_1)^2 + y^2}{\sigma_1^2} \Big) + \frac{\Gamma_1}{\pi\sigma_1^2} \exp\Big(- \frac{(x + 0.5b_1)^2 + y^2}{\sigma_1^2} \Big) \tag{5.2}$$

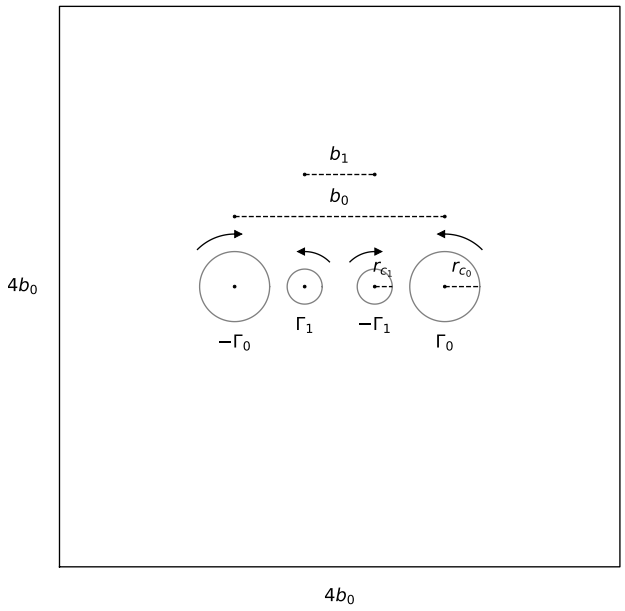

Figure 5.1: *Case representation : Four vortices of in a periodic box.*

The two initial situations at time $\tilde{t} = 0$ are represented in Figure 5.3. We can analyze the initial velocity profile as shown in Figure 5.2. When the vortex is in the opposite direction, $\Gamma_1 > 0$, we see that the downwash velocity in the center is higher and the upward peak of velocity is lower than in the case where there are only two vortices. If the primary and secondary vortices rotate in the same direction, $\Gamma_1 < 0$, two secondary maxima of velocity are created, replacing the maximum at $\tilde{x} = 0$. The result is a u-shaped function that is turned up instead of down. The upward maximum velocity is larger. Note that we can clearly see the center of the 2 secondary vortices at $\tilde{x} = \pm 0.25$.

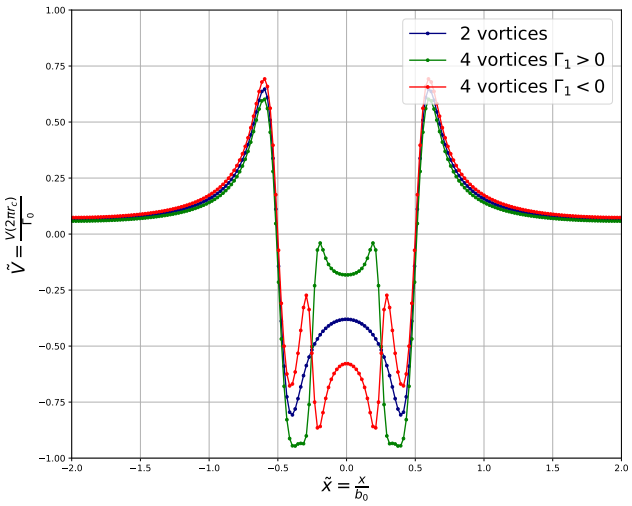

Figure 5.2: *Initial velocity profile $\tilde{V}(\tilde{x}, \tilde{y} = 0)$, simulated result for two vortices, four vortices with $\Gamma_1 > 0$ and four vortices with $\Gamma_1 < 0$ in a periodic domain of size $L = 4b_0$.*

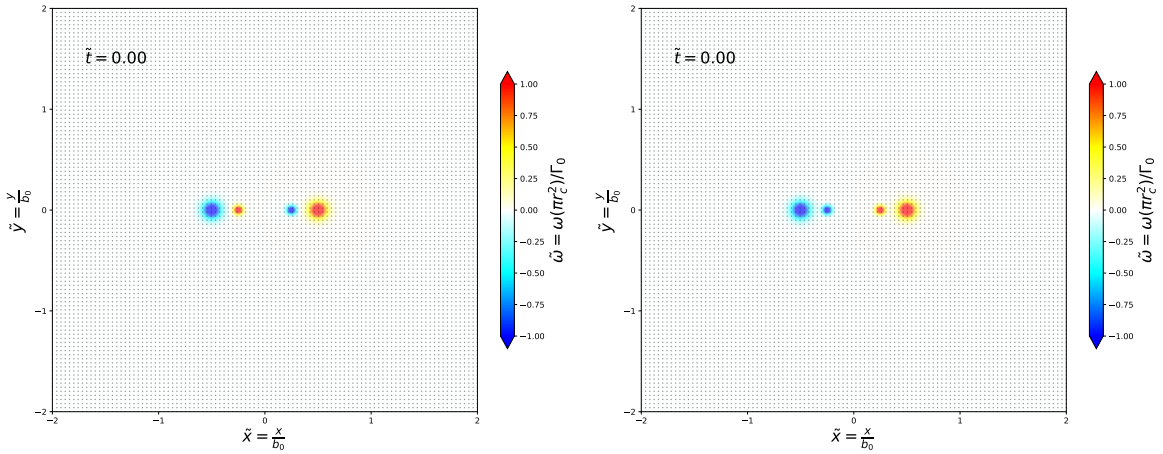

Figure 5.3: *Vorticity plot of the four vortices case at time $\tilde{t} = 0$ on a uniform grid with $\frac{h}{\sigma_0} = 0.113$. Left case is when $\Gamma_0, \Gamma_1 > 0$ and right case is when $\Gamma_0 > 0$ and $\Gamma_1 < 0$ with Γ_1 taken as in Figure 5.2. The light gray points correspond to the grid points, every fourth point is drawn.*

5.2 Analysis of the uniform results

We first presented the results for the situation where $\Gamma_1 > 0$ in Figure 5.5. We see that the vortices are repelled, the secondary vortex will rotate around the primary one. The first round of the smaller one around the larger one is performed in a dimensionless time of $\tilde{t} \approx 0.62$. The second in $\tilde{t} \approx 1.33$. We observe that the rotation speed decreases with time, this is due to diffusion. The small vortex will lose its circular shape to take a more stretched shape. This shape varies with time, compressing as it approaches the line $\tilde{x} = 0$, due to interaction with the other side of the system, and then stretching again as it moves away, see two bottom saturated plots in Figure 5.5. The primary vortex Γ_0 does not hold its position, it loops, then descends and loops again. This loop gets smaller over time, as shown in Figure 5.4 by examining the paths of the local extremum point (maximum or minimum value) of each vortex. We can see that the vortices are not getting closer to each other, but they are not moving away from each other either. The vortices are rotating together. If we look at the right side of the Figure 5.4, we can see that the system of two vortices will rotate around a point. But considering the whole system, the two right vortices will induce a downwash velocity on the left vortex, and the same inversely, this will create the special trajectory observed.

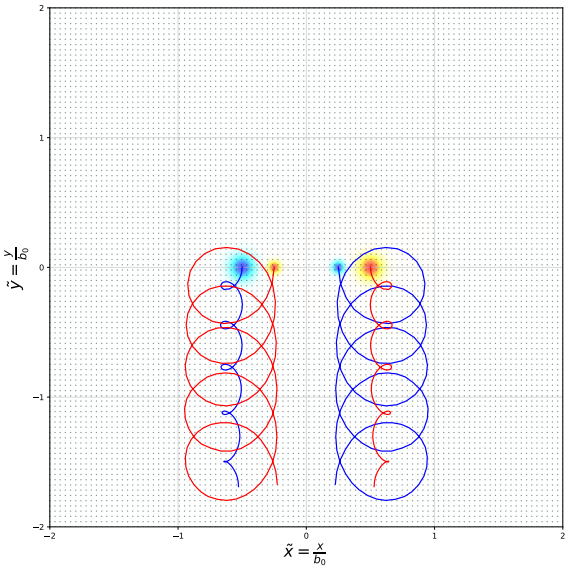

Figure 5.4: *Tracer of the position of the local extremum value of each vortex* ($\Gamma_1 > 0$) *for dimensionless time in* $\tilde{t} = [0, 3.67]$.

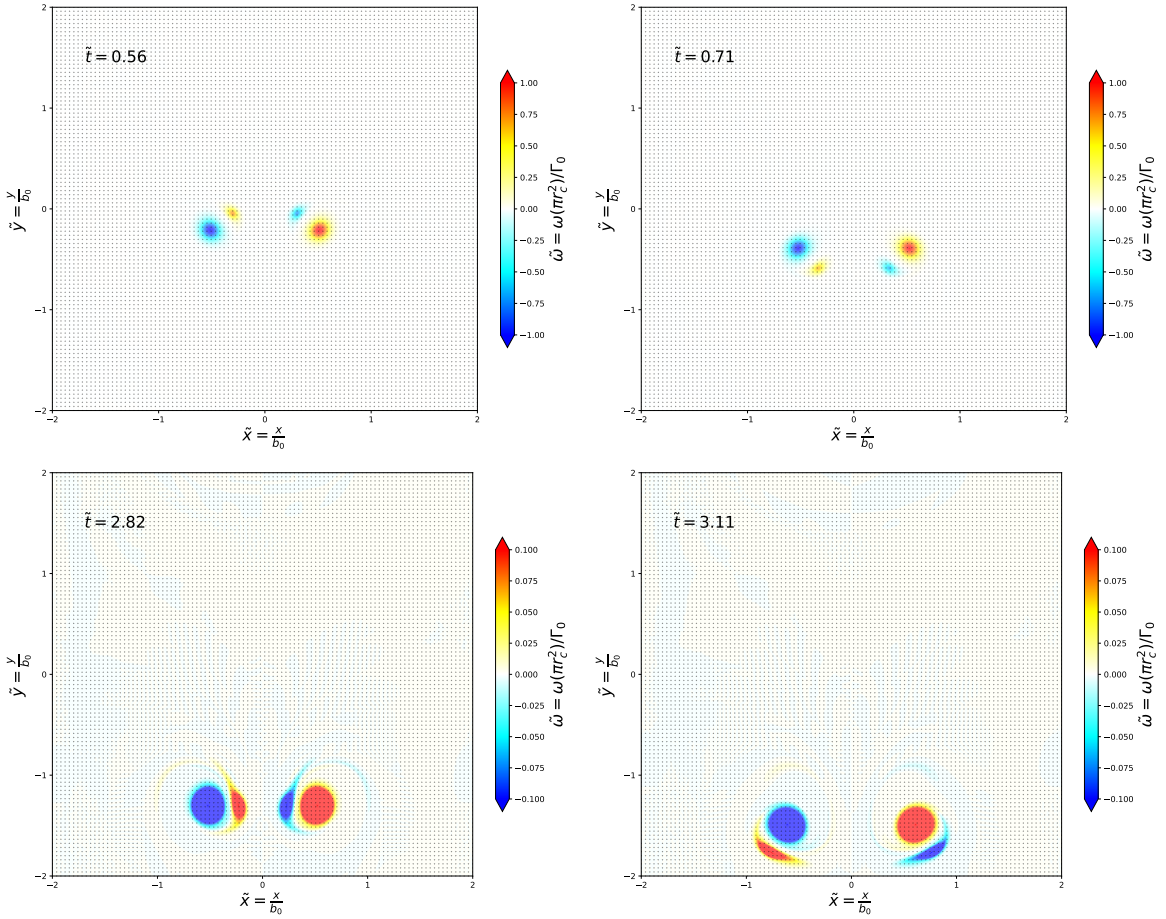

Figure 5.5: *Vorticity plot of the four vortices case* ($\Gamma_0 > 0$ *and* $\Gamma_1 > 0$) *with a non-uniform grid using mapping* 2 *and* $\frac{h}{\sigma_0} = 0.113$. *The two bottom plots are with a color plot saturated for* $|\tilde{w}| > 0.1$.

For the results of the $\Gamma_1 < 0$ case, we see that the small vortex is eaten by the large vortex to form a single large Gaussian vortex. The primary vortex filaments to absorb the secondary vortex. It is this filament that we will try to pass through the non-uniform mesh. Galaxies shape generated by the case are shown in Figure 5.6.

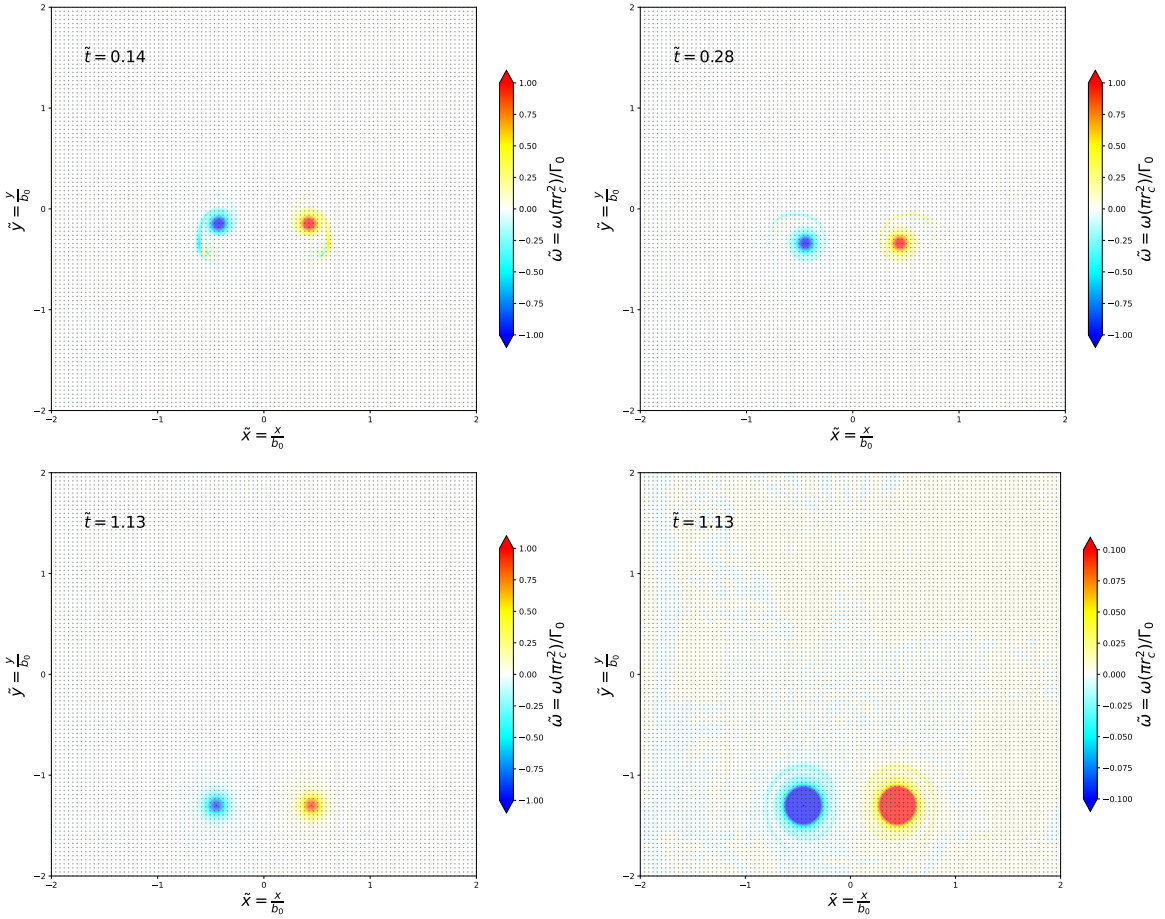

Figure 5.6: *Vorticity plot of the four vortices case* ($\Gamma_0 > 0$ *and* $\Gamma_1 < 0$) *with a non-uniform grid using mapping* 2 *and* $\frac{h}{\sigma_0} = 0.113$. *The right bottom plots is similar to the left bottom but with a color plot saturated for* $|\tilde{w}| > 0.1$.

5.3 Analysis of the non-uniform results with mitigation model

In the first case, the vortex around the main vortex rotates faster in the non-uniform case using mapping 2 than in the uniform case. This is shown in Figure 5.7 when comparing the time $\tilde{t} = 2.82$ and 3.11 with the uniform case shown in Figure 5.5. The error manifests itself by a wrong convection velocity of the secondary vortices. When applying the mitigation model $(CD_2 - CD_1CD_1)$ with $C = 1$ and $C = 1.5$, we observe no reduction of the error compared to the case without mitigation. This is due to the fact that dispersion errors do not manifest themselves in the form of oscillations, so hyperdiffusion mitigation term has no effect. In this case, the model is useless and the secondary vortex remains poorly convected. In Figure 5.8, we can see that the ∞- and 2-norm errors are almost the same regardless of the value of the mitigation coefficient C. This error is in the order of magnitude of the case as all the secondary

vortex positions are wrong. The conclusion is that our model and any high order derivatives mitigation term is useful in this case.

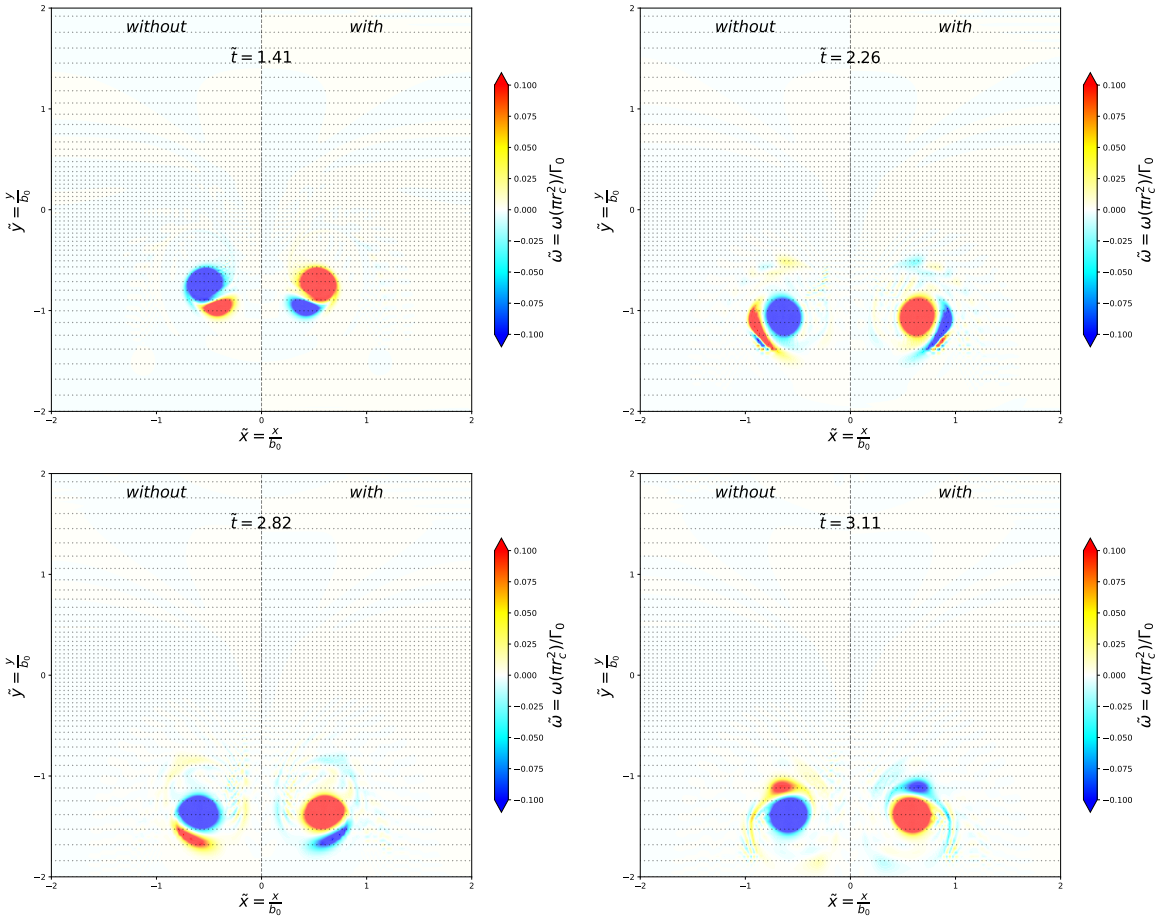

Figure 5.7: *Comparison of the dimensionless vorticity* $\tilde{w}$ *between case* $\Gamma_1 > 0$*, without and with mitigation term* $(C = 1)$ *going from* $\frac{\Delta}{\sigma_0} = 0.113$ *to* $\frac{\Delta}{\sigma_0} = 0.452$*. The color plot is saturated for* $|\tilde{\omega}| > 0.1$*.*

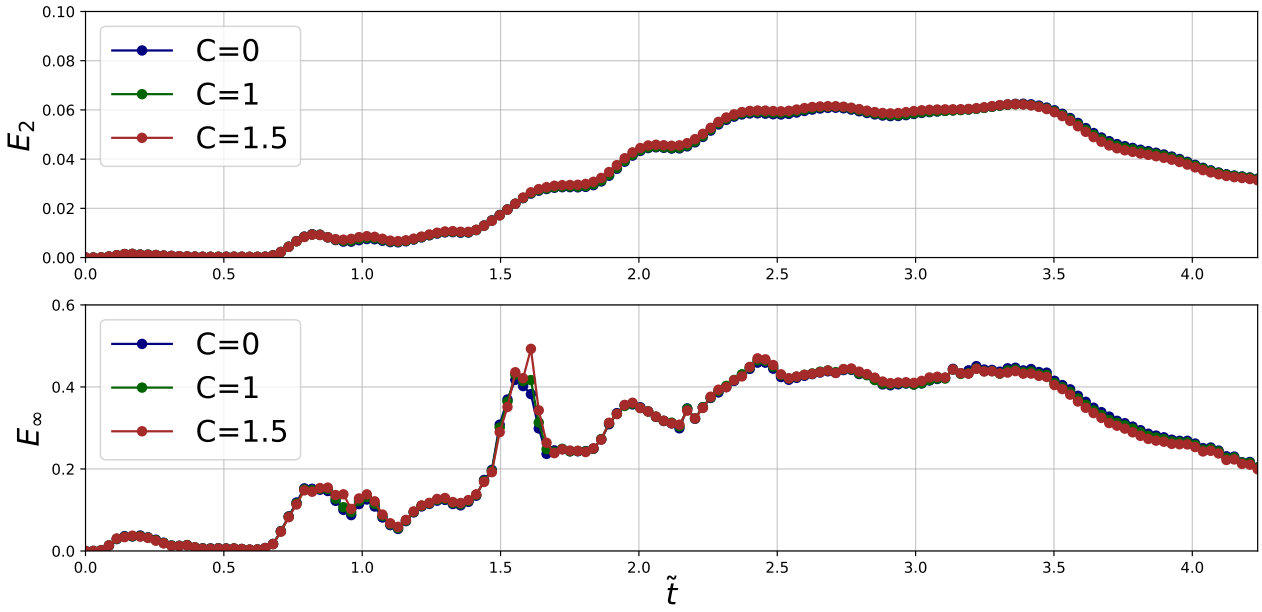

Figure 5.8: *Error plots (E_2 and E_∞) for the case $\Gamma_1 > 0$ as a function of the dimensionless time $\tilde{t}$ comparing the mitigation model ($CD_2 - CD_1CD_1$) for different values of C. When the value of C is set to 0 it means that there is no mitigation.*

For the second case, $\Gamma_1 < 0$, the vortex is correctly absorbed as in the variable resolution, as shown in the Figure 5.9. A small dispersion error is generated and takes a form similar to the two vortices case. Using a mitigation model ($CD_2 - CD_1CD_1$) with $C = 1$ the effect is correctly mitigated as shown in the error plots Figure 5.10. A value of C between 1 and 1.5 seems to be a good value. The first bump in the error is when the first filament is created, as shown for $\tilde{t} = 0.14$ in Figure 5.6. Then oscillations started after $\tilde{t} > 1$ and we observed an increase of the error in the base case $C = 0$. The use of the mitigation term has a positive effect, however, it can be seen that the model does not reconstruct the errors in the filament, as shown in the local error plot, Figure 5.11. We can see that for $\tilde{t} = 0.75$, the error when $C = 1.5$, the mitigation term generates new errors around the case. When $\tilde{t} > 0$, we see that $C = 1$ and $C = 1.5$, have almost the same result when comparing E_2 and E_∞, but in practice, $C = 1.5$ corrects the dispersion error better, but generates additional errors around the vortex. Even if the results are closed, we will prefer a value of C closer to 1 in this case, since we do not want to add another source of error.

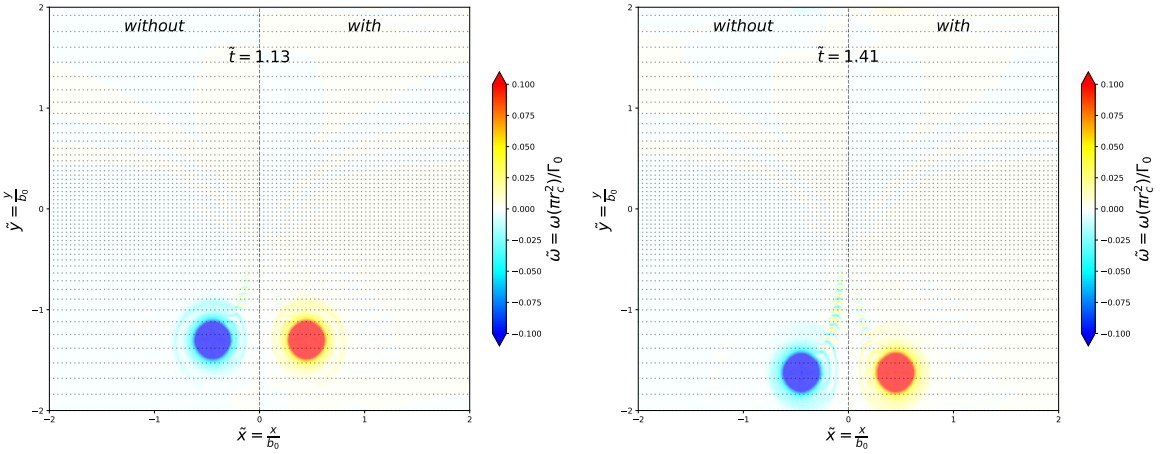

Figure 5.9: *Comparison of the dimensionless vorticity $\tilde{w}$ between case $\Gamma_1 < 0$ without and with mitigation term $(C = 1)$ going from $\frac{\Delta}{\sigma_0} = 0.113$ to $\frac{\Delta}{\sigma_0} = 0.452$. The color plot is saturated for $|\tilde{\omega}| > 0.1$.*

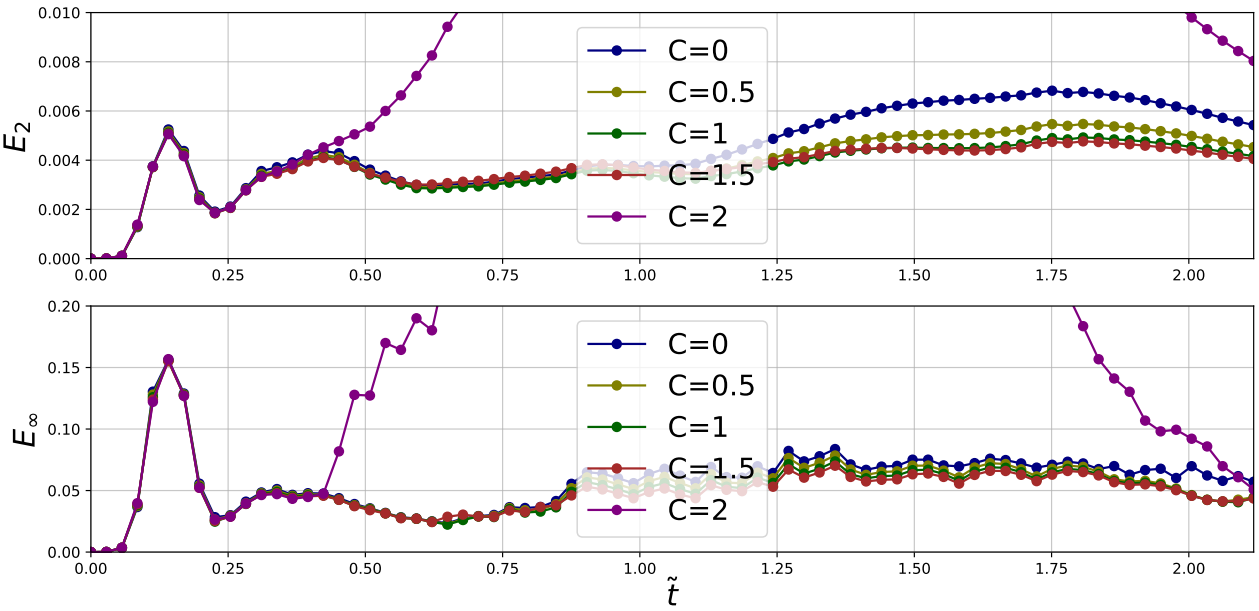

Figure 5.10: *Error plots (E_2 and E_∞) for the case $\Gamma_1 < 0$, as a function of the dimensionless time $\tilde{t}$ comparing the mitigation model $(CD_2 - CD_1CD_1)$ for different values of C. When the value of C is set to 0 it means that there is no mitigation.*

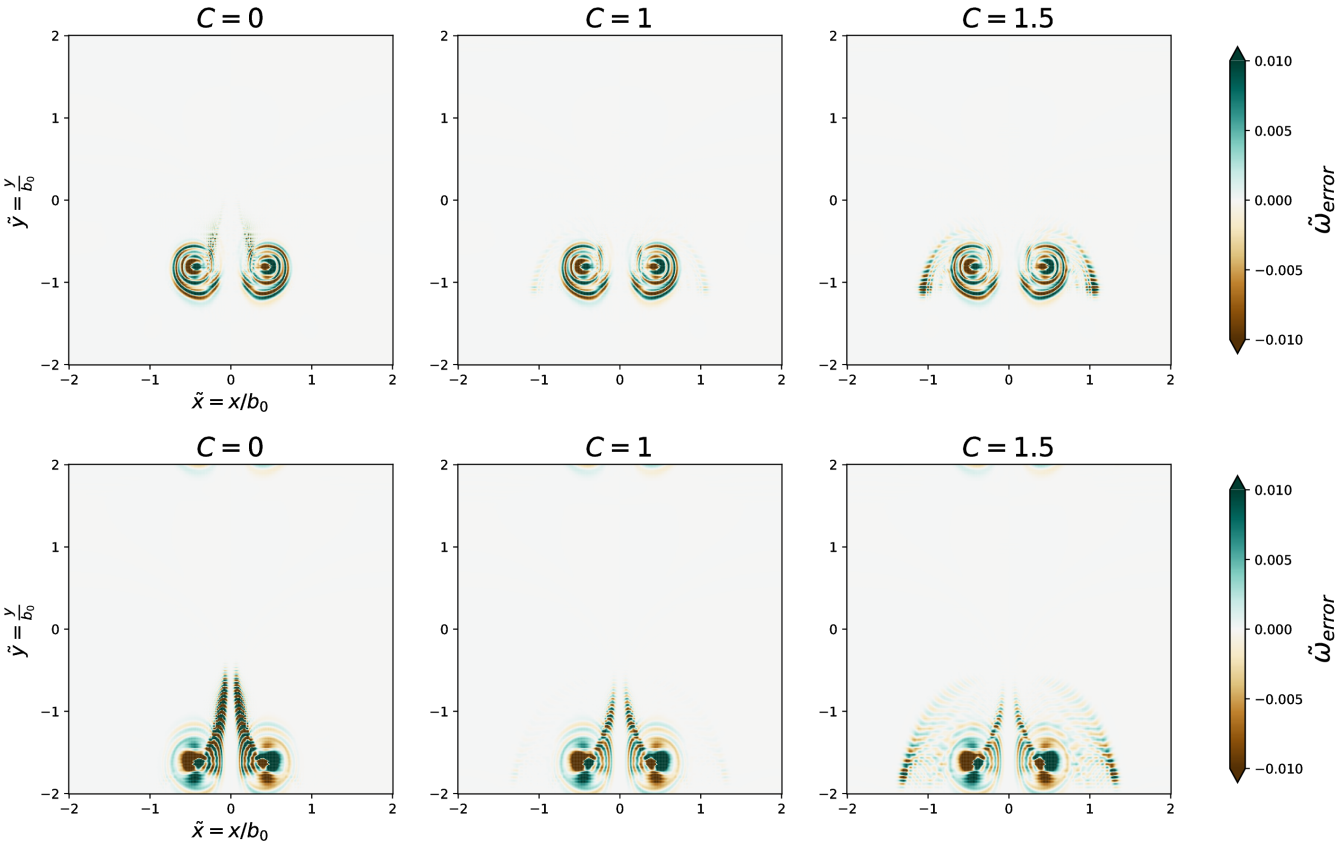

Figure 5.11: *Local error of the solver at time* $\tilde{t} = 0.75$ *(top) and* 1.41 *(bottom), the mapping 2 is used for the non-uniform case and the reference is an uniform simulation at* $\frac{h}{\sigma_0} = 0.113$*. The color plot is saturated at* 1% *of the dimensional vorticity* $\tilde{w}$*.*

We can therefore conclude that the model requires a well-chosen value for the coefficient C, depending on the case and the coarsening of the resolution. There is no exact formula that tells us the right value, different simulation must be performed. The best value can be taken by looking at errors in quantities such as vorticity or by comparing the error to a uniform case. The model is in fact a hyperdiffusion model, which is used to damp oscillations such as those resulting from dispersion errors. If the errors manifest themselves in some other form, such as an incorrect convection velocity of all a vorticity patch, the model has no effect. Furthermore, the model does not include the reconstruction of information lost through the transition to a less resolved discretization. There is no magic, no miracle cure, when information is lost, it is lost forever.

Chapter 6

Conclusion and perspectives

In this master's thesis, we have developed a Navier-Stokes finite difference solver with variable resolution. The spatial discretization is presented in detail through explanations of the MAC mesh, the "numerical" and "physical space" mapping functions, and the non-uniform discretization. Then the solver was demonstrated in two textbook cases, a flow past a cylinder and a Poiseuille flow. Next, we meticulously developed a case for the deep analysis of this thesis. The choosen case was two vortices in a periodic box. This enabled us to validate the order of the solver, the convection and the diffusion terms. We simulated the situation on a uniform resolution, a non-uniform resolution with a mapping with a discretization going to a twice coarse discretization, and a non-uniform resolution with a mapping with a discretization going to a four times coarse discretization. We were then able to investigate and quantify the dispersion errors when transitioning to the inhomogeneous mesh. In the next chapter, we present a mitigation term originally developed by [9] to correct for commutation errors in LES. The model has been dissected by explaining its discretization, the choice of coefficient and with a further development explaining hyperdiffusion. We have applied this term to our dispersion errors obtained in DNS with the two vortices case. We have seen that an intelligent choice of the coefficient can reduce the error. The model will correct the dispersion errors manifested by oscillations in the wake of the vortex. In the last chapter, we have made the case more complex by adding two secondary vortices. Two situations are considered. The first one is when the secondary vortices were of the opposite sign to the primary one. In this case, we observed that the error was not manifested by oscillations but by an incorrect convection of the secondary vortices. The mitigation model therefore has no impact on error corrections. The second one is when the secondary vortex has the same sign as the primary. The primary vortex will filament and absorb the secondary vortex. The error across the non-uniform discretization will manifest itself in two types. Errors in the filaments that are not corrected by the model and errors that manifest themselves as oscillations that are partially corrected by the model. In conclusion, we have seen that the model only attenuates oscillations. It is not miracoulus, it does not correct other types of error and it does not restore the information lost through mesh coarsement. What is more, the choice of the mitigation parameters must be made carefully, taking into account both the mapping function of the non-uniform discretization and the simulated case.

We have therefore been able to develop a hyperdiffusion model that reduces dispersion errors. Intuitively, when moving to a coarser resolution, one might think that information is lost and errors are created. Here we correct some of the errors by dissipating them in a more appropriate way, but we do not restore the lost information. The conclusion of this master's thesis is that it is more important to concentrate on an error-free simulation than to try to correct it. Spectral methods, for example, have negligible dispersion error, [47]. Higher-order methods with higher resolution have also limit errors, [48]. If we want to reconstruct the information lost, recently developed deep learning methods can close the problem and add back the physics lost by the coarsening [49, 50]. Unfortunately, in order to train the model, you need a lot of data from well-solved simulations or very precise experimental values. The mitigation model presented in this thesis and in paper [9] has an interest if it is impossible to use a finer model, and it can help to reduce some of the dispersion errors with a correct choice of the coefficient. It has been tested here in 2D with finite difference methods, but deserves further analysis in 3D and maybe using finite elements. Moreover, the model was initially developed for commutation errors in LES, so larger analysis can be envisaged there, even if, as mentioned in this master's thesis more important questions arise in LES [39]. Another way to continue the investigation of dispersion errors due to variable resolution done in this thesis would be to investigate and try to mitigate the errors that occur when a solver suddenly goes from a h resolution to a $2h$ resolution. The analysis could be used, for example, to improve multi-resolution methods [51].

We will finish this thesis by the citation of Benjamin Franklin, "An ounce of prevention is worth a pound of cure". In other words in French, "Mieux vaut prévenir que guérir".

Appendix A

Complete non-uniform discretization of the convection and diffusion terms

Here you can find the complete discretization of the advective and the divergence form used to create the skew-symmetric form of the convective term as well as the complete discretization of the diffusion term. The Navier-Stokes momentum equations can be written as

$$\frac{\partial u_i}{\partial t} + (Skew)_i = \nu(Diff)_i - (Pres)_i$$

Recall that

$$(Skew)_i = \frac{1}{2}(Adv)_i + \frac{1}{2}(Div)_i$$

And that the definition of Jx and Jy, the Jacobians that connect the "numerical space" to the "physical space", is

$$Jx(\xi_i) \approx \left.\frac{\delta x}{\delta \xi}\right|_i = \frac{x_{i+1/2} - x_{i-1/2}}{\Delta_\xi}$$

$$Jy(\eta_j) \approx \left.\frac{\delta y}{\delta \eta}\right|_j = \frac{y_{j+1/2} - y_{j-1/2}}{\Delta_\eta}$$

The discretization for the update of $u_{i,j-1/2}$ follows

$$\begin{aligned}
(Adv)_1 = {} & 0.25\Big((u_{i+1,j-1/2} + u_{i,j-1/2})\frac{(u_{i+1,j-1/2} - u_{i,j-1/2})}{Jx_{i+1/2}\Delta_\xi} + (u_{i,j-1/2} + u_{i-1,j-1/2})\frac{(u_{i,j-1/2} - u_{i-1,j-1/2})}{Jx_{i-1/2}\Delta_\xi}\Big) \\
& + 0.25\Big((v_{i+1/2,j} + v_{i-1/2,j})\frac{(u_{i,j+1/2} - u_{i,j-1/2})}{Jy_j\Delta_\eta} + (v_{i+1/2,j-1} + v_{i-1/2,j-1})\frac{(u_{i,j-1/2} - u_{i,j-3/2})}{Jy_{j-1}\Delta_\eta}\Big) \\
(Div)_1 = {} & \frac{0.25}{Jx_i\Delta_\xi}\Big((u_{i+1,j-1/2} + u_{i,j-1/2})(u_{i+1,j-1/2} + u_{i,j-1/2}) - (u_{i,j-1/2} + u_{i-1,j-1/2})(u_{i,j-1/2} + u_{i-1,j-1/2})\Big) \\
& + \frac{0.25}{Jy_{j-1/2}\Delta_\eta}\Big((v_{i+1/2,j} + v_{i-1/2,j})(u_{i,j+1/2} + u_{i,j-1/2}) - (v_{i+1/2,j-1} + v_{i-1/2,j-1})(u_{i,j-1/2} + u_{i,j-3/2})\Big)
\end{aligned}$$

$$(Diff)_1 = \frac{2}{(Jx_{i+1/2} + Jx_{i-1/2})\Delta_\xi}\Big(\frac{(u_{i+1,j-1/2} - u_{i,j-1/2})}{Jx_{i+1/2}\Delta_\xi} - \frac{(u_{i,j-1/2} - u_{i-1,j-1/2})}{Jx_{i-1/2}\Delta_\xi}\Big)$$
$$+ \frac{2}{(Jy_j + Jy_{j-1})\Delta_\eta}\Big(\frac{(u_{i,j+1/2} - u_{i,j-1/2})}{Jy_j\Delta_\eta} - \frac{(u_{i,j-1/2} - u_{i,j-3/2})}{Jy_{j-1}\Delta_\eta}\Big)$$

The discretization for the update of $v_{i-1/2,j}$ follows

$$(Adv)_2 = 0.25\Big((u_{i,j+1/2} + u_{i,j-1/2})\frac{(v_{i+1/2,j} - v_{i-1/2,j})}{Jx_i\Delta_\xi} + (u_{i-1,j+1/2} + u_{i-1,j-1/2})\frac{(v_{i-1/2,j} + v_{i-3/2,j})}{Jx_{i-1}\Delta_\xi}\Big)$$
$$+ 0.25\Big((v_{i-1/2,j+1} + v_{i-1/2,j})\frac{(v_{i-1/2,j+1} - v_{i-1/2,j})}{Jy_{j+1/2}\Delta_\eta} + (v_{i-1/2,j} + v_{i-1/2,j-1})\frac{(v_{i-1/2,j} - v_{i-1/2,j-1})}{Jy_{j-1/2}\Delta_\eta}\Big)$$
$$(Div)_2 = \frac{0.25}{Jx_{i-1/2}\Delta_\xi}\Big((u_{i,j+1/2} + u_{i,j-1/2})(v_{i+1/2,j} + v_{i-1/2,j}) - (u_{i-1,j+1/2} + u_{i-1,j-1/2})(v_{i-1/2,j} + v_{i-3/2,j})\Big)$$
$$+ \frac{0.25}{Jy_j\Delta_\eta}\Big((v_{i-1/2,j+1} + v_{i-1/2,j})(v_{i-1/2,j+1} + v_{i-1/2,j}) - (v_{i-1/2,j} + v_{i-1/2,j-1})(v_{i-1/2,j} + v_{i-1/2,j-1})\Big)$$

$$(Diff)_2 = \frac{2}{(Jx_i + Jx_{i-1})\Delta_\xi}\Big(\frac{(v_{i+1/2,j} - v_{i-1/2,j})}{Jx_i\Delta_\xi} - \frac{(v_{i-1/2,j} - v_{i-3/2,j})}{Jx_{i-1}\Delta_\xi}\Big)$$
$$+ \frac{2}{(Jy_{j+1/2} + Jy_{j-1/2})\Delta_\eta}\Big(\frac{(v_{i-1/2,j+1} - v_{i-1/2,j})}{Jy_{j+1/2}\Delta_\eta} - \frac{(v_{i-1/2,j} - v_{i-1/2,j-1})}{Jy_{j+1/2}\Delta_\eta}\Big)$$

Appendix B

Modal analysis of the second order finite difference schemes for first and second order derivatives

In this appendix, we will performed a detailed analysis of the modified wavenumber obtain with the centered second order finite difference schemes for first and second order derivatives [52]. To perform the modal analysis of the second order centered finite difference scheme for the convection equation, we start with the convection equation

$$\frac{\partial u}{\partial t} + c\frac{\partial u}{\partial x} = 0$$

Assuming a solution of the form $u(x,t) = A(t)e^{ikx}$, where $x_i = ih$ is the discrete location of the grid points and h is the spacial step size, we will examine and compare both the continuous and discretized forms of this equation. First, for the continuous form, we get

$$\frac{\partial}{\partial x}\left(A(t)e^{ikx}\right) = ikA(t)e^{ikx}$$

Consider the discretized form of the convection equation using a second order central finite difference scheme for the spatial derivative, also denoted as CD_1 in this thesis,

$$\left.\frac{\partial u}{\partial t}\right|_i = -c\left.\frac{\delta u}{\delta x}\right|_i = -c\frac{u_{i+1} - u_{i-1}}{2h}$$

For the assumed solution $u_i(t) = A(t)e^{ikx_i}$

$$u_{i+1}(t) = A(t)e^{ikx_{i+1}} = A(t)e^{ik(x_i+h)} = A(t)e^{ikx_i}e^{ikh}$$

$$u_{i-1}(t) = A(t)e^{ikx_{i-1}} = A(t)e^{ik(x_i-h)} = A(t)e^{ikx_i}e^{-ikh}$$

Substituting these into the discretized equation

$$\left.\frac{\delta u}{\delta x}\right|_i = \frac{A(t)e^{ikx_i}(e^{ikh} - e^{-ikh})}{2h}$$

Using Euler's formula $e^{ikh} - e^{-ikh} = 2i\sin(kh)$

$$\left.\frac{\delta u}{\delta x}\right|_i = \frac{i\sin(kh)}{h}A(t)e^{ikx_i}$$

Comparing the continuous convective term $-cikA(t)e^{ikx}$ with the discretized term $-ci\frac{\sin(kh)}{h}A(t)e^{ikx_i}$, we see that it involves a modified wavenumber which correponds to

$$k^* = \frac{\sin(kh)}{h}$$

We can also define the modified velocity which correspond to $c^* = \frac{ck^*}{k}$ and is given by

$$c^* = c\left(\frac{\sin(kh)}{kh}\right)$$

Evolution of k^* is shown on B.2. We see that low wavenumbers (low frequency) are correctly convected. For small kh, the term $\frac{\sin(kh)}{h}$ closely approximates k, indicating that the discretized form closely approximates the continuous convection equation. For larger kh, the term $\frac{\sin(kh)}{h}$ deviates from k, introducing numerical dispersion errors for high wavenumbers.

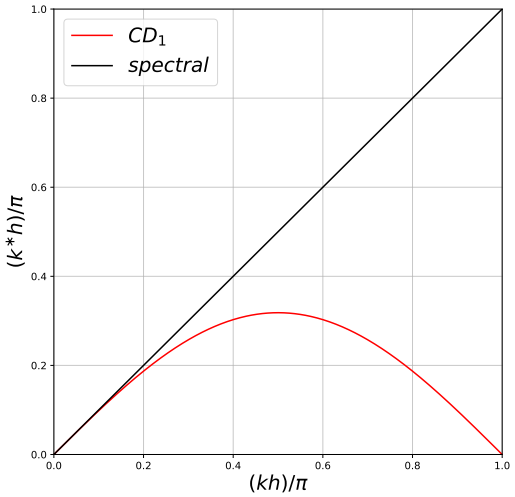

Figure B.1: *Modified wavenumber of the second order centered finite difference for first order derivative term.*

To compare the discretized form of the diffusion equation with the continuous form, let's assume a solution of the form $u(x,t) = A(t)e^{ikx}$ where $x_i = ih$ is the discrete location of the grid points and h is the spacial step size. First, consider the diffusion equation

$$\frac{\partial u}{\partial t} = \nu \frac{\partial^2 u}{\partial x^2}$$

For the assumed solution, the spatial second derivative is

$$\frac{\partial^2}{\partial x^2}\left(A(t)e^{ikx}\right) = -k^2 A(t)e^{ikx}$$

Now, consider the discretized form of the diffusion equation using the second order centered finite difference approximation, also called CD_2,

$$\left.\frac{\partial u}{\partial t}\right|_i = \nu \left.\frac{\delta^2 u}{\delta x^2}\right|_i = \nu \frac{u_{i+1} - 2u_i + u_{i-1}}{h^2}$$

For the assumed solution $u_i(t) = A(t)e^{ikx_i}$

$$u_{i+1}(t) = A(t)e^{ikx_{i+1}} = A(t)e^{ik(x_i+h)} = A(t)e^{ikx_i}e^{ikh}$$

$$u_{i-1}(t) = A(t)e^{ikx_{i-1}} = A(t)e^{ik(x_i-h)} = A(t)e^{ikx_i}e^{-ikh}$$

Substituting these into the discretized equation

$$\left.\frac{\delta^2 u}{\delta x^2}\right|_i = \nu A(t)e^{ikx_i}\frac{e^{ikh} - 2 + e^{-ikh}}{h^2}$$

Using Euler's formula $e^{ikh} + e^{-ikh} = 2\cos(kh)$

$$\left.\frac{\delta^2 u}{\delta x^2}\right|_i = \nu A(t)e^{ikx_i}\frac{2(\cos(kh) - 1)}{h^2}$$

Using the trigonometric identity for power-reducing formulas, $1 - \cos(kh) = 2\sin^2(kh/2)$, we get

$$\left.\frac{\delta^2 u}{\delta x^2}\right|_i = -\nu \frac{4\sin^2(kh/2)}{h^2} A(t)e^{ikx_i}$$

In the continuous case, the term $-\nu k^2 A(t)e^{ikx}$ describes the exact diffusion behavior. In the discretized form, the corresponding term is $-\nu\frac{4\sin^2(kh/2)}{h^2}A(t)e^{ikx_i}$. To see how well the discretized form approximates the continuous one, we will introduce the modified wavenumber

$$(k^2)^* = \frac{4\sin^2(kh/2)}{h^2}$$

Thus, for small kh, the discretized equation closely approximates the continuous diffusion equation. For larger kh, the term $\frac{4\sin^2(kh/2)}{h^2}$ deviates from k^2, introducing numerical dissipation errors.

The next scheme, denoted by (CD_1CD_1), is a second derivative scheme corresponding to the repeated application of the second order finite difference scheme for first derivative CD_1. This can also be considered as a second order centered finite difference CD_2 where we take $2h$ between points instead of h

$$\left.\frac{\delta^2 u}{\delta x^2}\right|_i = \nu \frac{u_{i+2} - 2u_i + u_{i-2}}{4h^2}$$

The modified wavenumber becomes in this case

$$(k^2)^* = \frac{\sin^2(kh)}{h^2}$$

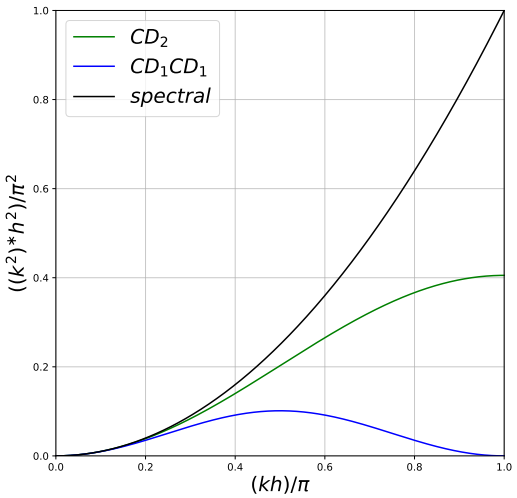

Figure B.2: *Modified wavenumber of the second order centered finite difference for the second order derivative term and the two successive applications of the second order centered finite difference for the first order derivative.*

Appendix C

Complete discretization of the mitigation model for $N = 4$ and $N = 6$ for a finite difference solver with a non-uniform grid

For $N = 4$, we will provide a detailed discretization of the model used for $F_4(u)$ called $(CD_2 - CD_1CD_1)u$ for the y direction as it is this used in this thesis.

The discretization for the update of $u_{i,j-1/2}$ is given by,

$$(CD_2)_{i,j-1/2} = \frac{2}{(Jy_j + Jy_{j-1})\Delta_\eta}\Big(\frac{(u_{i,j+1/2} - u_{i,j-1/2})}{Jy_j\Delta_\eta} - \frac{(u_{i,j-1/2} - u_{i,j-3/2})}{Jy_{j-1}\Delta_\eta}\Big)$$

$$(CD_1)_{i,j-1/2} = \frac{2}{(Jy_j + Jy_{j-1})}\Big(\frac{u_{i,j+1/2} - u_{i,j-3/2}}{2\Delta_\eta}\Big)$$

$$(CD_1CD_1)_{i,j-1/2} = \frac{2}{(Jy_j + Jy_{j-1})}\Big(\frac{(CD_1)_{i,j+1/2} - (CD_1)_{i,j-3/2}}{2\Delta_\eta}\Big)$$

For $v_{i-1/2,j}$ we have,

$$(CD_2)_{i-1/2,j} = \frac{2}{(Jy_{j+1/2} + Jy_{j-1/2})\Delta_\eta}\Big(\frac{(v_{i-1/2,j+1} - v_{i-1/2,j})}{Jy_{j+1/2}\Delta_\eta} - \frac{(v_{i-1/2,j} - v_{i-1/2,j-1})}{Jy_{j-1/2}\Delta_\eta}\Big)$$

$$(CD_1)_{i-1/2,j} = \frac{2}{(Jy_{j+1/2} + Jy_{j-1/2})}\Big(\frac{u_{i-1/2,j+1} - u_{i-1/2,j-1}}{2\Delta_\eta}\Big)$$

$$(CD_1CD_1)_{i-1/2,j} = \frac{2}{(Jy_{j+1/2} + Jy_{j-1/2})}\Big(\frac{(CD_1)_{i-1/2,j+1} - (CD_1)_{i-1/2,j-1}}{2\Delta_\eta}\Big)$$

For $N = 6$, we will provide a detailed discretization of the model $(CD_2^3)u$ that approximation $F_6(u)$.

For the update of $u_{i,j-1/2}$ we have,

$$(CD_2)_{i,j-1/2} = \frac{2}{(Jy_j + Jy_{j-1})\Delta_\eta}\Big(\frac{(u_{i,j+1/2} - u_{i,j-1/2})}{Jy_j\Delta_\eta} - \frac{(u_{i,j-1/2} - u_{i,j-3/2})}{Jy_{j-1}\Delta_\eta}\Big)$$

$$(CD_2^2)_{i,j-1/2} = \frac{2}{(Jy_j + Jy_{j-1})\Delta_\eta}\Big(\frac{((CD_2)_{i,j+1/2} - (CD_2)_{i,j-1/2})}{Jy_j\Delta_\eta} - \frac{((CD_2)_{i,j-1/2} - (CD_2)_{i,j-3/2})}{Jy_{j-1}\Delta_\eta}\Big)$$

$$(CD_2^3)_{i,j-1/2} = \frac{2}{(Jy_j + Jy_{j-1})\Delta_\eta}\Big(\frac{((CD_2^2)_{i,j+1/2} - (CD_2^2)_{i,j-1/2})}{Jy_j\Delta_\eta} - \frac{((CD_2^2)_{i,j-1/2} - (CD_2^2)_{i,j-3/2})}{Jy_{j-1}\Delta_\eta}\Big)$$

For $v_{i-1/2,j}$ we have,

$$(CD_2)_{i-1/2,j} = \frac{2}{(Jy_{j+1/2} + Jy_{j-1/2})\Delta_\eta}\Big(\frac{(v_{i-1/2,j+1} - v_{i-1/2,j})}{Jy_{j+1/2}\Delta_\eta} - \frac{(v_{i-1/2,j} - v_{i-1/2,j-1})}{Jy_{j-1/2}\Delta_\eta}\Big)$$

$$(CD_2^2)_{i-1/2,j} = \frac{2}{(Jy_{j+1/2} + Jy_{j-1/2})\Delta_\eta}\Big(\frac{((CD_2)_{i-1/2,j+1} - (CD_2)_{i-1/2,j})}{Jy_{j+1/2}\Delta_\eta} - \frac{((CD_2)_{i-1/2,j} - (CD_2)_{i-1/2,j-1})}{Jy_{j-1/2}\Delta_\eta}\Big)$$

$$(CD_2^3)_{i-1/2,j} = \frac{2}{(Jy_{j+1/2} + Jy_{j-1/2})\Delta_\eta}\Big(\frac{((CD_2^2)_{i-1/2,j+1} - (CD_2^2)_{i-1/2,j})}{Jy_{j+1/2}\Delta_\eta} - \frac{((CD_2^2)_{i-1/2,j} - (CD_2^2)_{i-1/2,j-1})}{Jy_{j-1/2}\Delta_\eta}\Big)$$

Bibliography

[1] A. Saint-Amand, J. Lambrechts, C. Thomas, and E. Hanert. How fine is fine enough? effect of mesh resolution on hydrodynamic simulations in coral reef environments. *Ocean Modelling*, 186:102254, 2023.

[2] D-G. Caprace, P. Chatelain, and G. Winckelmans. Wakes of rotorcraft in advancing flight: A large-eddy simulation study. *Physics of Fluids*, 32(8):087107, 2020.

[3] P. Soni, S. Kumar, B. Kumar, et al. A comprehensive review on cfd simulations of left ventricle hemodynamics: numerical methods, experimental validation techniques, and emerging trends. *J. Braz. Soc. Mech. Sci. Eng.*, 46:301, 2024.

[4] J. Jacob and P. Sagaut. Wind comfort assessment by means of large eddy simulation with lattice boltzmann method in full scale city area. *Building and Environment*, 139:110–124, 2018.

[5] G. Winckelmans, M. Duponcheel, L. Bricteux, I. De Visscher, and O. Thiry. Turbulent vortex pair at equilibrium and its interaction with the ground at $re_\Gamma = 2 \times 10^5$. *Journal of Fluid Mechanics*, 987:A34, 2024.

[6] C. Fefferman. Existence and Smoothness of the Navier-Stokes Equation. In James Carlson, Arthur Jaffe, and Andrew Wiles, editors, *The Millennium Prize Problems*, pages 57–67. American Mathematical Society and Clay Mathematics Institute, Providence, RI, 2006.

[7] C. Johnson. *Numerical Solution of Partial Differential Equations by the Finite Element Method*. Cambridge University Press, 1987.

[8] A. Kolmogorov. Local structure of turbulence in an incompressible fluid at very high reynolds numbers. *Dokl. Akad. Nauk SSSR*, 30:301–305, 1941.

[9] G. Yalla, T. Oliver, S. Haering, B. Engquist, and R. Moser. Effects of resolution inhomogeneity in large-eddy simulation. *Phys. Rev. Fluids*, 6:074604, 2021.

[10] G. Winckelmans. LMECA2660 : Numerical methods in fluid dynamics. UCLouvain, 2023.

[11] S. Balay, S. Abhyankar, M. Adams, S. Benson, J. Brown, et al. PETSc Web page, 2024. URL `https://petsc.org/`.

[12] J. Welch, F. Harlowand J. Shannon, and J. Daly. The mac method-a computing technique for solving viscous, incompressible, transient fluid-flow problems involving free surfaces. 1965.

[13] S. McKee, M.F. Tomé, V.G. Ferreira, J.A. Cuminato, A. Castelo, F.S. Sousa, and N. Mangiavacchi. The mac method. *Computers Fluids*, 37(8):907–930, 2008.

[14] Y. Morinishi, T. Lund, O. Vasilyev, and P. Moin. Fully conservative higher order finite difference schemes for incompressible flow. *Journal of Computational Physics*, 143:90–124, 1998.

[15] O. Vasilyev. High order finite difference schemes on non-uniform meshes with good conservation properties. *Journal of Computational Physics*, 157(2):746–761, 2000.

[16] R. Morrow and L. Cram. Flux-corrected transport and diffusion on a non-uniform mesh. *Journal of Computational Physics*, 57(1):129–136, 1985.

[17] O. Vasilyev and N. Kevlahan. Hybrid wavelet collocation–brinkman penalization method for complex geometry flows. *International Journal for Numerical Methods in Fluids*, 40:531 – 538, 2002.

[18] T. Von Kármán. *Aerodynamics*. McGraw-Hill Book Company, Incorporated, 1957.

[19] P. Koumoutsakos and A. Leonard. High-resolution simulations of the flow around an impulsively started cylinder using vortex method. *Journal of Fluid Mechanics*, 296:1–38, 1995.

[20] P. Billuart, M. Duponcheel, G. Winckelmans, and P. Chatelain. A weak coupling between a near-wall eulerian solver and a vortex particle-mesh method for the efficient simulation of 2d external flows. *Journal of Computational Physics*, 473:111726, 2023.

[21] S. Sutera and R. Skalak. The history of poiseuille's law. *Annual Review of Fluid Mechanics*, 25:1–20, 11 2003.

[22] P. Chatelain, A. Curioni, M. Bergdorf, D. Rossinelli, W. Andreoni, and P. Koumoutsakos. Billion vortex particle direct numerical simulations of aircraft wakes. *Computer Methods in Applied Mechanics and Engineering*, 197(13):1296–1304, 2008.

[23] D-G. Caprace, G. Winckelmans, P. Chatelain, and J. Eldredge. *Wake Vortex Detection and Tracking for Aircraft Formation Flight.*

[24] D-G. Caprace, S. Buffin, M. Duponcheel, P. Chatelain, and G. Winckelmans. Large eddy simulation of advancing rotor for near to far wake assessment. 2017.

[25] T. Leweke, S. Le Dizès, and C. Williamson. Dynamics and instabilities of vortex pairs. *Annual Review of Fluid Mechanics*, 48:507–541, 2016.

[26] J. Gabbard, T. Gillis, P. Chatelain, and W. van Rees. An immersed interface method for the 2D vorticity-velocity Navier-Stokes equations with multiple bodies. *Journal of Computational Physics*, 464:111339, 2022.

[27] A. Salih. Streamfunction-vorticity formulation. Technical report, Department of Aerospace Engineering, Indian Institute of Space Science and Technology, Thiruvananthapuram, 2013.

[28] E. Weinan and L. Jian-Guo. Vorticity boundary condition and related issues for finite difference schemes. *Journal of Computational Physics*, 124(2):368–382, 1996.

[29] P. Chatelain et al. Formation flight: wake sensing and assessment of hazard for external traffic. In *TFM ASA 2022*, 2022.

[30] V. Meleshkoand G. van Heijst. On chaplygin's investigations of two-dimensional vortex structures in an inviscid fluid. *Journal of Fluid Mechanics*, 272:157–182, 1994.

[31] V. Brion, D. Sipp, and L. Jacquin. Linear dynamics of the Lamb-Chaplygin dipole in the two-dimensional limit. *Physics of Fluids*, 26(6):064103, 2014.

[32] T. Gillis, Y. Marichal, G. Winckelmans, and P. Chatelain. A 2d immersed interface vortex particle-mesh method. *Journal of Computational Physics*, 394:700–718, 2019.

[33] R. Moser, S. Haering, and G. Yalla. Statistical properties of subgrid-scale turbulence models. *Annual Review of Fluid Mechanics*, 53(Volume 53, 2021):255–286, 2021.

[34] S. Ghosal and P. Moin. The basic equations for the large eddy simulation of turbulent flows in complex geometry. *Journal of Computational Physics*, 118(1):24–37, 1995.

[35] D. Carati, G. Winckelmans, and H. Jeanmart. On the modelling of the subgrid-scale and filtered-scale stress tensors in large-eddy simulation. *Journal of Fluid Mechanics*, 441: 119–138, 2001.

[36] J. Smagorinsky. General circulation experiments with the primitive equations: I. the basic experiment. *Monthly Weather Review*, 91(3):99 – 164, 1963.

[37] H. Jeanmart and G. Winckelmans. Comparison of recent dynamic subgrid-scale models in the case of the turbulent channel flow. In *Proceedings of the Center for Turbulence Research Summer Program 2002*, pages 105–116. Stanford University & NASA Ames, 2002.

[38] H. Jeanmart and G. Winckelmans. Investigation of eddy-viscosity models modified using discrete filters: A simplified "regularized variational multiscale model" and an "enhanced field model". *Physics of Fluids - PHYS FLUIDS*, 19, 2007.

[39] J. Volker. *Large Eddy Simulation of turbulent incompressible flows. Analytical and mumerical results for a class of LES models*, volume 34. 2004.

[40] A. Pahlavan, L. Cueto-Felgueroso, A. Hosoi, G.H. McKinley, and R. Juanes. Thin films in partial wetting: stability, dewetting and coarsening. *Journal of Fluid Mechanics*, 845: 642–681, 2018.

[41] A. Pahlavan, L. Yang, C. Bain, and H. Stone. Evaporation of binary-mixture liquid droplets: The formation of picoliter pancakelike shapes. *Phys. Rev. Lett.*, 127:024501, 2021.

[42] C. Taylor. Finite difference coefficients calculator, 2016. URL `https://web.media.mit.edu/~crtaylor/calculator.html`.

[43] J. McWilliams. A demonstration of the suppression of turbulent cascades by coherent vortices in two-dimensional turbulence. *Physics of Fluids A: Fluid Dynamics*, 2(4):547–552, 1990.

[44] H. Clercx and G. van Heijst. Two-Dimensional Navier-Stokes turbulence in bounded domains. *Applied Mechanics Reviews*, 62, 2009.

[45] M. Gazzola, P. Chatelain, W. van Rees, and P. Koumoutsakos. Simulations of single and multiple swimmers with non-divergence free deforming geometries. *Journal of Computational Physics*, 230(19):7093–7114, 2011.

[46] L. Bricteux, M. Duponcheel, and G. Winckelmans. A multiscale subgrid model for both free vortex flows and wall-bounded flows. *Physics of Fluids*, 21(10):105102, 10 2009.

[47] D. Gottlieb and S. Orszag. *Numerical Analysis of Spectral Methods*. Society for Industrial and Applied Mathematics, 1977.

[48] O.C. Zienkiewicz, R.L Taylor, and J.Z. Zhu. *The Finite Element Method: Its Basis and Fundamentals*. Elsevier Science, 2005.

[49] S. Rudy, S. Brunton, J. Proctor, and N. Kutz. Data-driven discovery of partial differential equations. *Science Advances*, 3(4):e1602614, 2017.

[50] A. Gupta and P. Lermusiaux. Neural closure models for dynamical systems. *Proceedings of the Royal Society A: Mathematical, Physical and Engineering Sciences*, 477:20201004, 2021.

[51] M. Wenhua, L. Dongmi, L. Shiyi, Q. Jianxian, N. Guoxi, and C. Yibing. High-order adaptive multi-resolution method on curvilinear grids i: Finite difference framework. *Journal of Computational Physics*, 498:112654, 2024.

[52] J. Strikwerda. *Finite Difference Schemes and Partial Differential Equations, Second Edition*. Society for Industrial and Applied Mathematics, 2004.

UNIVERSITÉ CATHOLIQUE DE LOUVAIN
École polytechnique de Louvain
Rue Archimède, 1 bte L6.11.01, 1348 Louvain-la-Neuve, Belgique | **www.uclouvain.be/epl**